Influence of ~~Major~~ Sudden Stratospheric Warming With Elevated Stratopause on the Hydroxyl in the Polar Middle Atmosphere

Jin Hu[1], Sheng-Yang Gu[1*], Yusong Qin[1*], Yuxuan, Liu[1], and Yafei Wei[1]
[1]School of Earth and Space Science and Technology, Wuhan University, Wuhan, China
*Corresponding author: Sheng-Yang Gu (gushengyang@whu.edu.cn) & Yusong Qin (qinyusong@whu.edu.cn), School of Earth and Space Science and Technology, Wuhan University, Wuhan, China.

Abstract: Based on the specified dynamics simulation of Whole Atmosphere Community Climate Model with ionosphere/thermosphere extension (SD-WACCM-X), the composite response of polar Hydroxyl (OH) layer in the mesosphere and lower thermosphere (MLT) to the Arctic ~~major~~ sudden stratospheric warming (SSW) events with elevated stratopause (ES) during 2004-2023 is investigated. A total of ten ES-SSW events are systematically analyzed. Before the onset of ES-SSW events, the OH concentration climatologically peaks at 7.4×10^{-9} mol/mol near ~82.4 km. During the stratospheric warming phase, relative to the climatology, the peak height of OH layer undergoes a distinct upward displacement reaching ~85.9 km accompanied by a reduction in the OH concentration to 2.9×10^{-9} mol/mol. This shift is closely linked to an ~11% and ~90.8% reduction in mesospheric temperature and atomic oxygen, respectively, due to enhanced upward residual circulation. During the elevated stratopause phase, the peak height of OH layer experiences a pronounced downward shift to ~80.6 km with a maximum in OH concentration to 6.8×10^{-9} mol/mol. This phase is characterized by ~3.7% and ~137.3% enhancements in mesospheric temperature and atomic oxygen concentrations, respectively, which is driven by intensified downward residual circulation. Further analysis suggests that OH concentration variations are positively correlated to mesospheric temperature anomalies and atomic oxygen redistribution induced by vertical transport, which is attributed to the significant influence of ES-SSW on gravity wave drag (GWs) in the mesosphere.

Key Points

1. The peak height of Arctic OH layer rises during the stratospheric warming phase and descends during the elevated stratopause phase.
2. The change in OH concentration during ES-SSW shows a significant positive correlation with the change in mesospheric atomic oxygen concentration and temperature.
3. The vertical circulation anomalies due to the variations in gravity wave drag during ES-SSW alter the mesospheric atomic oxygen concentration and temperature.

1. Introduction

The middle atmosphere, spanning from ~20 to 100 km in altitude, plays a vital role in coupling different atmospheric layers and modulating space weather phenomena. Hydroxyl (OH) is a key component in the MLT region, exerting an essential function in atmospheric chemistry and serving as an important indicator for assessing the atmospheric thermal budget. In the mesopause region, OH is primarily produced through the reaction between ozone and atomic hydrogen, forming excited OH* near 87 km. This excited state is deactivated either via photon emission in the Meinel bands (observed as nightglow) or by collisional quenching. The latter process prevails at lower altitudes, where higher atmospheric density facilitates the formation of a ground-state OH layer near 82 km (Damiani et al., 2010).

Despite the relatively well-understood chemical formation of OH, comprehensive observational characterization of its variability remains limited. Nevertheless, measurements from ground-based instruments and satellites, such as Thermosphere Ionosphere Mesosphere Energetics and Dynamics (TIMED)/Sounding of the Atmosphere using Broadband Emission Radiometry (SABER) and Aura Microwave Limb Sounder (MLS), have provided a valuable opportunity to examine OH variability (Gao et al., 2011; Damiani et al., 2010; Medvedeva et al., 2019). Shapiro et al. (2012) identified a positive correlation between mesospheric OH variability and 27-day solar irradiance cycles, with stronger responses observed during periods of heightened solar activity. Minschwaner et al. (2011) further demonstrated that ultraviolet actinic flux serves as the primary driver of OH diurnal variability. Li et al. (2005) observed that OH

concentrations peak near local noon, followed by a pronounced decline during nighttime. Additionally, statistical analyses by Gao et al. (2016; 2011; 2010) on the temporal and spatial distributions of OH and O_2 nightglow emissions highlighted significant local time variations, seasonal dependencies, hemispheric asymmetries, and a strong dependence on solar activity. Grygalashvyly et al. (2021) examined the semi-annual variation of the excited OH emission layer at mid-latitudes, attributing the results to the semi-annual oscillation of atomic oxygen and temperature.

Among the most prominent dynamical phenomena in the middle atmosphere are stratospheric sudden warmings (SSW), a large-scale wintertime phenomenon characterized by a rapid stratospheric temperature increase, zonal wind reversal, and substantial disruptions in atmospheric circulation (Manney et al., 2008; Chen et al., 2016; Bolaji et al., 2016; Gu et al., 2021). Studies have shown that SSW events are able to greatly modulate variations of atmospheric chemistry parameters (e.g., Kumar et al., 2024), particularly OH concentration (e.g., Winick et al., 2009). For example, Winick et al. (2009) attributed variations in OH layer to concurrent changes in temperature and atomic oxygen concentration in the upper mesosphere during the winters of 2004 and 2006. Similarly, Gao et al. (2011) documented reductions in OH and O_2 emissions associated with the January 2009 SSW, whereas Medvedeva et al. (2019) identified longitudinal disparities in OH emissions during the January 2013 SSW, which were likely modulated by variations in vertical wind patterns.

In certain cases, particularly following SSW events, an elevated stratopause (ES) may form, marked by an anomalously large ascent in stratopause height (Manney et al., 2008; Limpasuvan et al., 2016). Unlike typical SSW events, ES-SSWs can induce stronger and longer-lasting disturbances that extend well into the MLT, leading to enhanced traveling planetary wave activity, altered thermal structures, and significant changes in mesospheric chemical composition, including OH concentration (Qin et al., 2024; Rhodes et al., 2021; Tweedy et al., 2013). Nevertheless, the investigations into the impacts of ES-SSWs on polar mesospheric chemistry remain limited due to the sparse sampling of satellite observations, as exemplified by the TIMED/SABER satellite, which follows a precession orbit and requires several days to achieve full local time coverage. As a result, the influences of ES-SSWs on polar mesospheric OH

concentration remain insufficiently understood.

Numerical simulations offer an alternative approach for investigating variations in the OH layer under dynamically complex conditions. The Specified Dynamics Whole Atmosphere Community Climate Model with ionosphere/thermosphere eXtension (SD-WACCM-X) offers a physically consistent representation of mesospheric chemistry and dynamics, allowing for a more continuous and spatially resolved analysis of OH layer responses to ES-SSW events. Previous studies have successfully employed SD-WACCM-X to investigate atmospheric dynamics procession (e.g., Zhang et al., 2025; Orsolini et al., 2022), which demonstrates that the SD-WACCM-X simulations provide a valuable opportunity for capturing OH variations during ES-SSWs in the absence of comprehensive observational coverage.

This study aims to explore the responses of OH concentrations to ES-SSW events using the SD-WACCM-X simulations for the period 2004–2023. Section 2 provides a brief introduction to the datasets, the definition of ES-SSW, and the analysis methods used in this study. Section 3 presents the results, focusing on the peak values and peak height of OH concentrations, along with their temporal evolution in response to ES-SSW events. Section 4 discusses the roles of mesospheric temperature and atomic oxygen in changes of OH layer and the underlying mechanisms of OH concentration variations during ES-SSW events. Finally, Section 5 summarizes the key findings and their implications for mesospheric dynamics during ES-SSWs.

2. Data and Method

2.1 SD-WACCM-X

In this study, the Whole Atmosphere Community Climate Model with ionosphere/thermosphere eXtension (WACCM-X; Liu et al., 2018), an extended version of WACCM embedded within the Community Earth System Model version 2.2.0 (CESM2.2.0) framework developed by the National Center for Atmospheric Research (NCAR) (Gettelman et al., 2019; Danabasoglu et al., 2020), is employed to consider the characteristics of OH layer in the polar mesosphere. WACCM-X is an atmospheric model that simulates atmospheric processes from the surface (~0 km) up to the ionosphere/thermosphere, extending to ~700 km depending on solar activity, which provides a detailed representation of dynamic, chemical, and radiative processes

in the stratosphere, mesosphere, and thermosphere. The WACCM-X used in this study is based on the Community Atmosphere Model-6 (CAM-6) physics and the three-dimensional chemical transport Model for Ozone and Related chemical Tracers (MOZART) chemistry (Gettelman et al., 2019). Specifically, WACCM-X incorporates nonorographic gravity wave drag parameterization, solar and geomagnetic forcing, and comprehensive gas and aerosol chemistry (Lee et al., 2021). The middle atmosphere scheme with the D-region chemistry (MAD) is used.

The specified dynamics (SD) configuration of WACCM-X is nudged by Modern-Era Retrospective Analysis for Research and Applications Version 2 (MERRA-2) data (e.g., Molod et al., 2015; Teng et al., 2021) to ensure consistency with observed meteorological conditions. Both chemical and dynamical parameters in SD-WACCM-X are relaxed toward linearly time-interpolated 3-hourly MERRA-2 reanalysis data. The relaxation coefficient is uniform below 50 km, decreases progressively above this altitude, and becomes zero above 60 km (Brakebusch et al., 2013). Consequently, the model is unconstrained by reanalysis above 60 km. The vertical resolution of the model ranges from ~1.1 km to ~3.5 km, with a vertical density of two points per scale height below ~50 km and increasing to four points per scale height above ~50 km (Salinas et al., 2023). Enhanced vertical resolution in the troposphere and stratosphere enables improved representation of key physical processes (Sassi and Liu, 2014). The horizontal resolution is typically set to 1.9° × 2.5° (latitude×longitude). It should be noted that CESM currently provides emission input files for the SD-WACCM-X only up to the year 2015 (https://svn-ccsm-inputdata.cgd.ucar.edu/trunk/inputdata/atm/cam/chem/emis/CMIP6_emissions_1750_2015_2deg). Accordingly, prescribed emissions from CESM input were used prior to 2015, while for subsequent years, the emission fields were set to missing values. Sensitivity tests~~(Figure S1)~~ conducted for representative pre-2015 years (2009, 2010, and 2013) demonstrate that this treatment has a negligible impact on the simulated OH response to SSW (Figure S1), thereby ensuring the robustness of our results.

SD-WACCM-X simulations have been demonstrated to effectively reproduce observed atmospheric responses to ES-SSW events (e.g., Limpasuvan et al., 2016; Lee et al., 2021; Zhang et al., 2021; Zhang et al., 2025; Orsolini et al., 2022). These

successes highlight the model's robustness in capturing the dynamical and chemical processes, particularly within the MLT. In this study, model outputs spanning the period from 2004 to 2023 are utilized, with data from December through March extracted for each year, corresponding to the climatological window during which ES-SSW events predominantly occur. To comprehensively elucidate the response of the OH layer on ES-SSW, key variables such as OH, atomic oxygen, temperature, zonal wind, and so on are output. From these outputs, daily means of relevant dynamical and chemical parameters are derived to facilitate temporal-spatial evaluation of ES-SSW responses.

OH emission measurements from the SABER instrument onboard the TIMED satellite (https://saber.gats-inc.com/data.php) are employed to validate the SD-WACCM-X simulation. TIMED satellite was launched on 7 December 2001 and began SABER observations in early 2002. SABER provides global limb observations of OH airglow in the mesosphere and lower thermosphere, with latitude coverage alternating every 60 days between 53° and 83° in the opposite hemisphere (Gao et al., 2011, 2016).

2.2 Definition of SSW and ES Events

According to the criteria established by McInturff (1978), a major SSW is identified when, at 10 hPa or below, the latitudinal mean temperature must increase poleward of 60° latitude, accompanied by a reversal in the zonal-mean zonal winds (i.e., a transition from mean westerly to mean easterly winds poleward of 60° latitude). However, the definition of major SSWs has evolved over the decades and varies across studies, ranging from Northern Annular Mode index values (Baldwin and Dunkerton, 2001) to classifications emphasizing vortex morphology (Charlton and Polvani, 2007), or disturbances centered near the stratopause (~50 km) rather than the canonical 10 hPa level (Tweedy et al., 2013; Stray et al., 2015; Limpasuvan et al., 2016). Given these inconsistencies, we define the SSW onset as the day when the temperature difference between 60°N and 90°N at 10 hPa becomes positive, a diagnostic also adopted in ~~(e.g.,~~ Ma et al.~~,~~ (2020).

An elevated stratopause (ES) event is phenomenologically characterized as a disruption~~refers to a phenomenon~~ in which the winter polar stratopause initially descends, then becomes indistinct, and eventually reforms at a much higher altitude than usual (Chandran et al., 2013). Despite this descriptive definition, the diagnostic

criteria for identifying ES events remain ambiguous, with different studies applying different thresholds. For example, Torre et al. (2012) required the newly reformed stratopause to be displaced by more than 15 km relative to its original altitude, whereas Tweedy et al. (2013) and Harvey et al. (2025) used a threshold of a polar-cap stratopause elevation exceeding 10 km. ~~The newly reformed stratopause is displaced by more than 15 km compared to its original altitude (Torre et al., 2012).~~ In this study, any upward displacement of the stratopause relative to its pre-warming altitude is regarded as an ES event. Based on this criterion, ten ES-SSW events are identified over 2004-2023, including the 2010, 2018, 2021, and 2023 cases, which exhibited relatively modest elevations but are consistently classified as ES-SSW, in agreement with earlier studies (e.g., Harvey et al., 2025; Schneider et al., 2025; Harada et al., 2019). The stratopause height is defined as the altitude of maximum temperature within the 20-100 km vertical domain (Chandran et al., 2013). Nearly all identified ES events in our study are associated with major SSWs, with the only exception being the 2012 case, which followed a minor warming but still exhibited a pronounced elevated stratopause.

~~The stratopause height is defined as the altitude of maximum temperature within the 20-100 km vertical domain (Chandran et al., 2013). ES events are frequently observed in connection with major SSW events. According to the criteria established by McInturff (1978)the World Meteorological Organization (WMO), a major SSW is identified: at 10 hPa or below, the latitudinal mean temperature must increase poleward of 60° latitude, accompanied by a reversal in the zonal-mean zonal winds (i.e., a transition from mean westerly to mean easterly winds poleward of 60° latitude). (Baldwin and Dunkerton, 2001)(Charlton and Polvani, 2007)(Tweedy et al., 2013; Stray et al., 2015; Limpasuvan et al., 2016)~~

~~–~~To develop a statistically robust understanding of the OH layer characteristics during ES-SSW, a composite analysis is conducted by temporally aligning each event such that Day 0 corresponds to the SSW onset~~, defined as the day when the eastward wind reverses to a westward wind at 50 km with the maximum reversed wind~~. This alignment allows for a systematic examination of the temporal evolution and spatial structure of OH layer during ES-SSW events, providing insights into their common features and variability. In this study, the response of OH layer to ES-SSW events is

categorized into three distinct stages based on the temporal evolution of temperature: Day -15 to Day 0 is considered the normal stage; Day 0 to Day 5 correspond to the stratosphere warming stage; Day 6 to Day 60 correspond to the elevated stratopause stage.

3. Results

The SSW event that commenced in January 2009 started as the strongest, most prolonged on record, and isolated, which has been made a focal point for numerous studies (e.g., Manney et al., 2009; Yue et al., 2010; Limpasuvan et al., 2011). These unique characteristics render it particularly suitable for employing the response of mesospheric chemical composition to SSW events. The response of OH concentrations to ES-SSW events is exemplified by the 2009 SSW case, as illustrated in Figure 1. From top to bottom, Figure 1 represents (a) zonal-mean temperature at 10 hPa (~32 km) and 80° N, (b) zonal-mean wind at 60° N, (c) ~~and~~ temporal variations in OH concentrations at latitudes 75~90° N from SD-WACCM-X, and (d) in OH emission at 75-77° N from SABER during January 6, 2009, to March 22, 2009. In Figure 1a, the meridional temperature difference between 60°N and 90°N~~gradient~~ ($T[80^\circ - 90^\circ] - T[60^\circ - 70^\circ]$ K) is denoted by the pink solid line, and the ~~height of the ES~~ stratopause height is indicated by the green dashed line.

Prior to January 10, 2009, the temperature peak is located at 61 km, with a maximum ~272 K. Subsequently, the peak height drops sharply, reaching ~37.7 km by January 21, 2009. Between January 21 and January 26, 2009, the minimum temperature of 183.5 K occurs at altitudes above 75 km, while the meridional temperature difference between 60°N and 90°N at 10 hPa transitions to positive values. After January 26, 2009, a new stratopause forms at 86 km, with an upward displacement of ~~51~~25 km compared to the stratopause altitude before January 10, 2009, and subsequently descends to its climatological altitude in conjunction with the recovery of the polar vortex (Limpasuvan et al., 2012). This elevated stratopause event is accompanied by a pronounced downwelling over the winter pole, extending from 45 to 95 km. The enhanced subsidence facilitates the downward transport of MLT air into the stratosphere, thereby modulating the thermal structure and influencing polar chemical processes.

Figure 1b depicts the zonal mean wind changes at 60° N. Before the SSW onset,

the zonal mean wind is eastward with a speed of ~85 m/s. During the stratosphere warming phase, the zonal mean flow reverses to westward winds (below 0 m/s) in the polar winter stratosphere, confirming the occurrence of a major SSW event. Subsequently, the zonal-mean wind structure during the elevated stratopause exhibits a pattern similar to that of the zonal-mean temperature, with eastward winds prevailing in the mesosphere region at ~91.8 m/s. As the polar vortex recovers, the eastward wind gradually descends to its climatological distribution, mirroring the temperature evolution in the stratosphere and mesosphere.

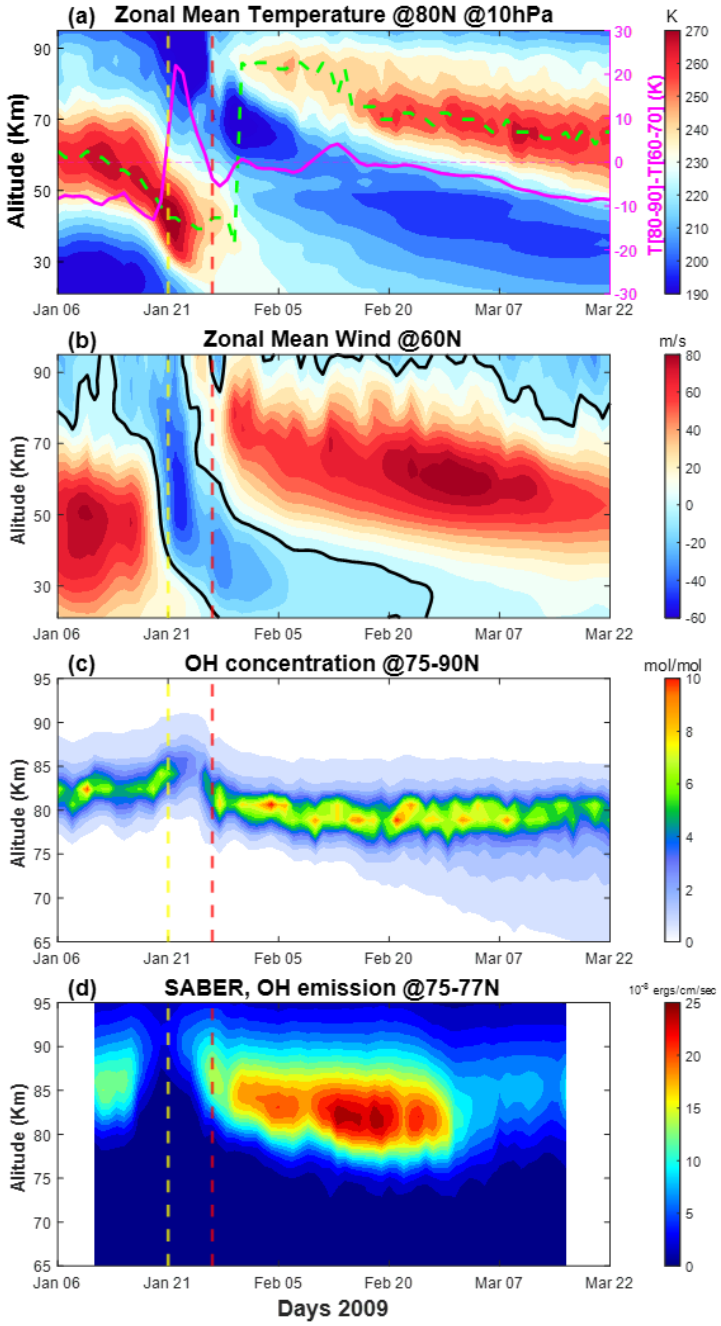
(a) Zonal Mean Temperature @80N @10hPa
K
Alitude (Km)
T[80-90]-T[60-70] (K)
(b) Zonal Mean Wind @60N
m/s
Alitude (Km)
(c) OH concentration @75-90N
mol/mol
Alitude (Km)
(d) SABER, OH emission @75-77N
10⁻⁶ ergs/cm/sec
Alitude (Km)
Jan 06
Jan 21
Feb 05
Feb 20
Mar 07
Mar 22
Days 2009

259

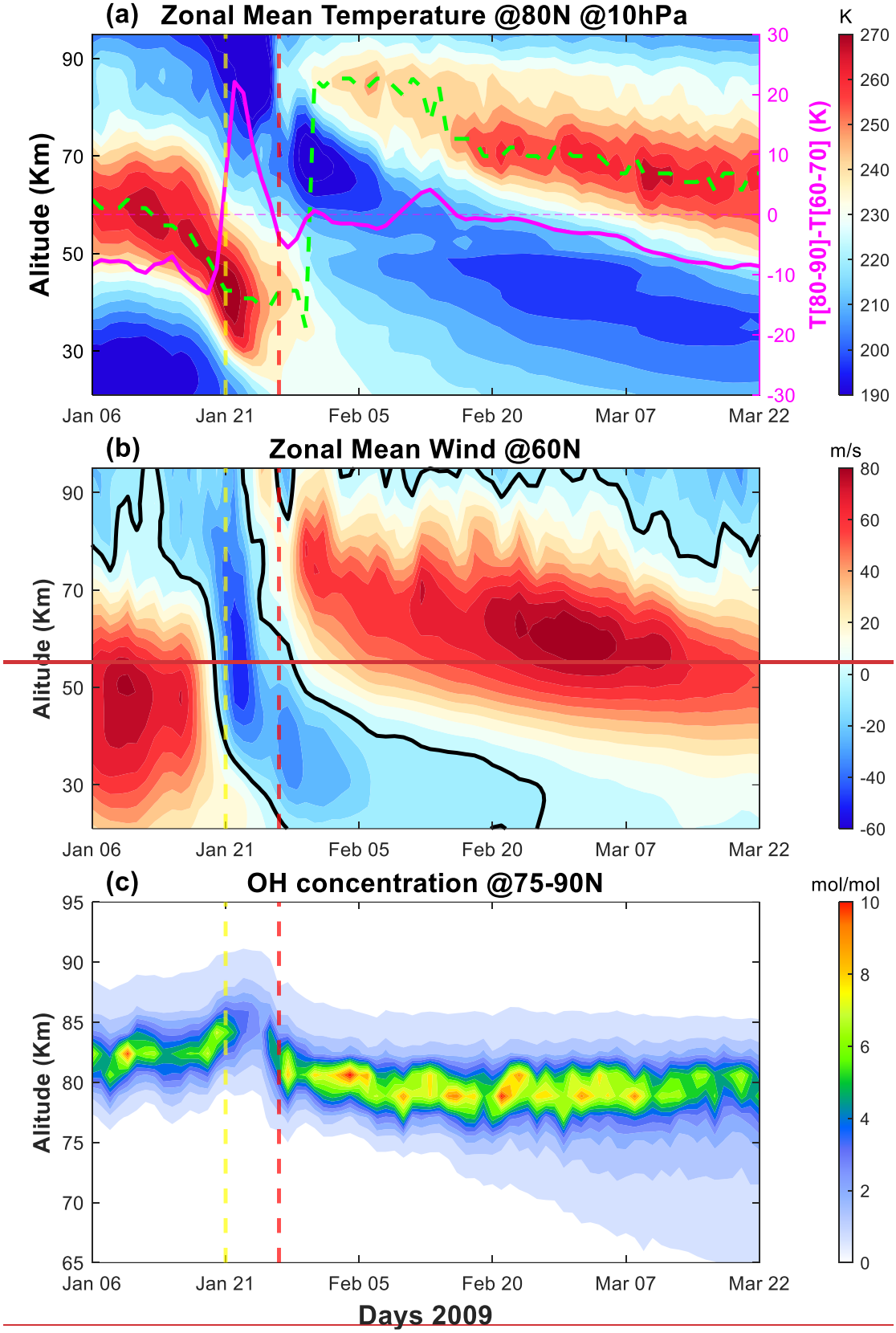

Figure 1. Time-altitude cross-section of SD-WACCM-X zonal-mean (a) temperature at 80°N, (b) zonal wind at 60°N, ~~and~~ (c) OH concentration (in units

of 10^{-9}), and SABER (d) OH emission, –during January 06-March 22, 2009. The solid pink line represents the meridional temperature difference between 60°N and 90°N ($T[80^\circ - 90^\circ] - T[60^\circ - 70^\circ]$), and the dashed green line is the stratopause height. The black solid contour in (b) denotes the zero-wind line. Vertical dashed yellow and red lines are the onset of the stratosphere warming stage and elevated stratopause stage, respectively.

Figure 1c illustrates the temporal variation of OH concentration during the 2009 events. Prior to the onset, the OH concentrations remain ~7.2×10^{-9} mol/mol with a peak height ~82.4 km. However, between January 21 and January 26, 2009, a pronounced depletion in OH concentrations is observed reaching a minimum of ~2.35×10^{-9} mol/mol, while the peak altitude shifts upward to 86 km. Following January 26, 2009, the peak of OH concentrations exhibits a gradual increase, eventually surpassing the pre-SSW levels and reaching values of ~10.6×10^{-9} mol/mol. This enhanced concentration persisted and did not return to its climatological level until March 9, 2009. These fluctuations align with findings from other studies (Gao et al., 2011; Winick et al., 2009). The SABER-retrieved OH airglow distribution is depicted in Figure 1d, whose temporal pattern closely resembles the SD-WACCM-X simulation due to their common production pathway. Nevertheless, a systematic offset exists in the altitude of the peak layer, where the altitude of peak OH airglow (~87 km) typically lies slightly above the peak of ground-state OH (~82km). This difference arises because SABER measured radiative emissions from vibrationally excited OH (v>0), whereas SD-WACCM-X output reflects the total OH concentration dominated by ground-state OH (v=0). –

Table 1 Onset Day (Day 1 corresponds to January 1 of the Year) of the ES-SSW Events During Boreal Winter of 2004~2023

Years	Onset day	Years	Onset day
2003/2004	Jan 2	2012/2013	Jan 5
2005/2006	Jan 9	2017/2018	Feb 14
2008/2009	Jan 21	2018/2019	Dec 25
2009/2010	Jan 20	2020/2021	Jan 2
2011/2012	Jan 11	2022/2023	Feb 13

Note. ES-SSW, sudden stratosphere warming with elevated stratopause.

To further validate the observed response of OH concentrations to ES-SSW events, SSW occurrences from 2004 to 2023 are analyzed, aiming to identify common characteristics across multiple events. Based on the criteria outlined in the methodology section, a total of ten ES-SSW events are identified (Manney et al., 2008; Maute et al., 2014; Kodera et al., 2008; Manney et al., 2009; Harada et al., 2010; Jones et al., 2018; Chandran et al., 2013; Goncharenko et al., 2013; De Wit et al., 2014; Karpechko et al., 2018; Rao et al., 2019; Okui et al., 2021; Lu et al., 2021; Qin et al., 2024; Zhang et al., 2025), with their occurrence years and onset dates listed in Table 1. The left column of the table indicates the years in which ES-SSW events occurred, while the right column specifies the first day of each event.

Figure 2 presents the temporal variations in OH concentrations for each selected year, centered on the onset day of the ES-SSW event and spanning from 15 days prior to 60 days after the onset. As shown, during the stratosphere warming phase, the peak height of OH concentration undergoes an evident upward displacement to ~86 km, whereas the OH concentrations peak experiences a sharp decline with the minimum of ~1×10^{-9}-2×10^{-9} mol/mol. Conversely, during the elevated stratopause phase, as the peak height of the OH layer significantly decreases, the peak OH concentration increases rapidly to ~7×10^{-9}~9×10^{-9} mol/mol at 78 km, and its maximum is larger than that in the normal stage. The results reveal a consistent pattern similar to that shown in Figure 1c, demonstrating that the influence of ES-SSW events on OH concentration is a common feature across all identified occurrences. In certain years, i.e., 2010, 2018, and 2023, the influence of ES-SSW events on the structure of OH concentration appears weaker, potentially due to variations in event intensity or background atmospheric conditions. Furthermore, although SSW events vary in their duration and intensity, they tend to occur on an annual basis. Some events occur in close succession, as observed in 2008, whereas others appear as isolated episodes, such as the one in 2009. During ES-SSW events, preceding or subsequent SSW-related mesospheric warming and elevated stratopause phases remain active, introducing additional modulation to the observed OH variations.

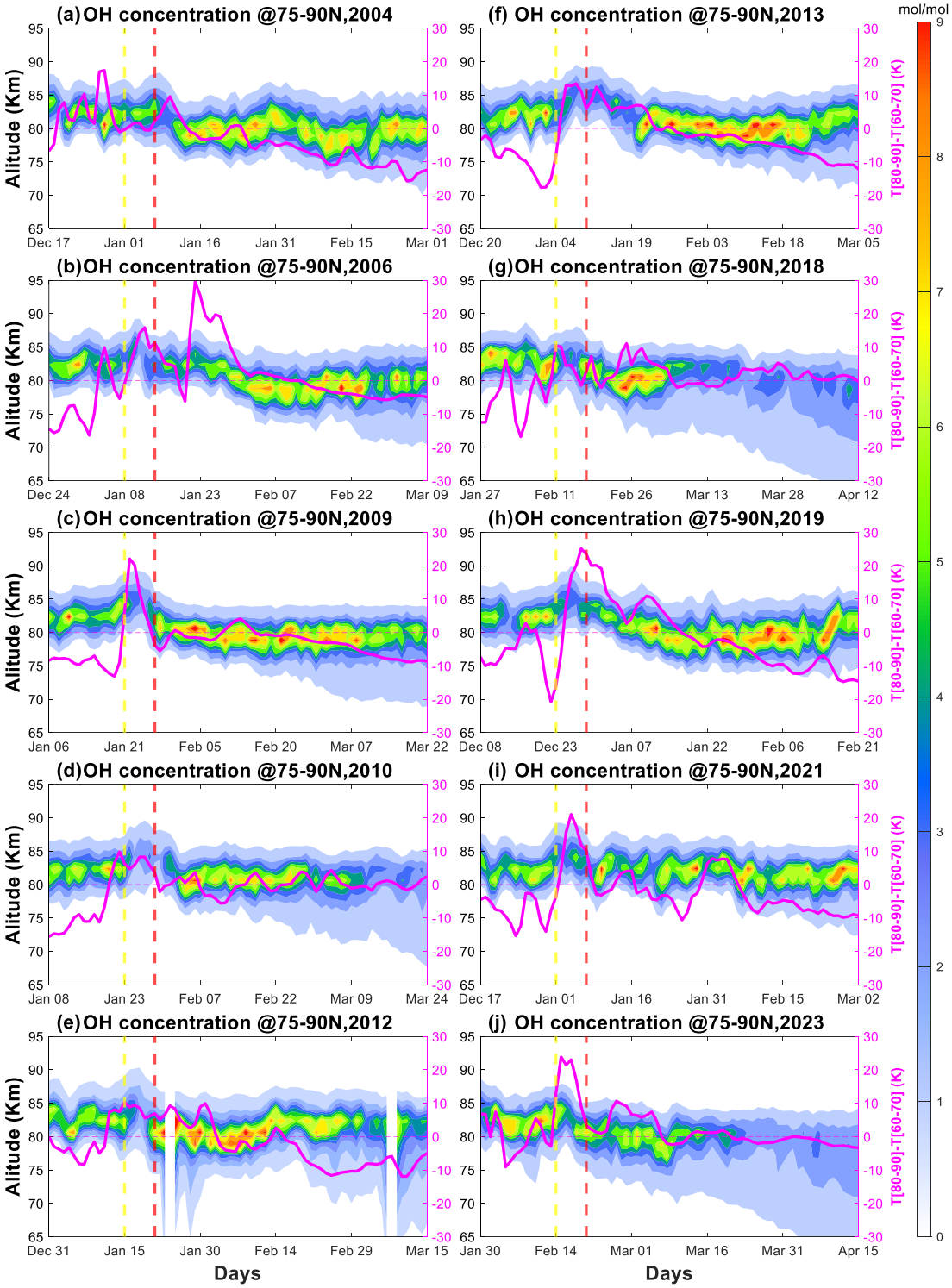

Figure 2. Time-altitude cross-sections of OH concentrations (in units of 10^{-9}) in ES-SSW events during 2004-2023 are captured in panels a-j. The solid pink line represents the meridional temperature difference between 60°N and 90°N ($T[80^\circ-90^\circ]-T[60^\circ-70^\circ]$). Vertical dashed yellow and red lines are the onset of the stratosphere warming stage and elevated stratopause stage, respectively.

Notably, OH concentrations in some SSW events such as February 2010 and 2023, also show a significant downward extension in altitude after March, suggesting that seasonal variability may play a noticeable role in the temporal evolution of OH concentrations. As illustrated in Figure 3, OH concentrations display a clear seasonal pattern, with higher values in the summer hemisphere (May to August in the Northern Hemisphere; November to February in the Southern Hemisphere) and lower values in the winter hemisphere.~~illustrates the seasonal evolution in OH concentrations in both the Northern and Southern Hemispheres. The OH concentration exhibits a clear seasonal pattern, with higher values in the summer hemisphere (May to August in the Northern Hemisphere; November to February in the Southern Hemisphere) and lower values in the winter hemisphere.~~ The peak of OH concentration in the summer hemisphere reaches ~12.5×10^{-9} mol/mol, whereas the minimum OH concentration in the winter hemisphere is ~5×10^{-9} mol/mol. Additionally, the seasonal cycle also modulates the vertical structure of the OH layer: in summer, OH extends broadly from ~75 km to ~87 km, whereas in winter it is confined near ~82.5 km. This summer broadening helps explain the downward extension of OH observed during late-winter sudden stratospheric warming events, such as those in 2010 and 2023.~~the vertical distribution of OH concentration varies across different seasons. In the summer hemisphere, the OH concentration extends over a broader altitude range, from ~75 km to ~87 km. In contrast, in the winter hemisphere, the OH peak is more confined, occurring at an altitude of ~82.5 km.~~

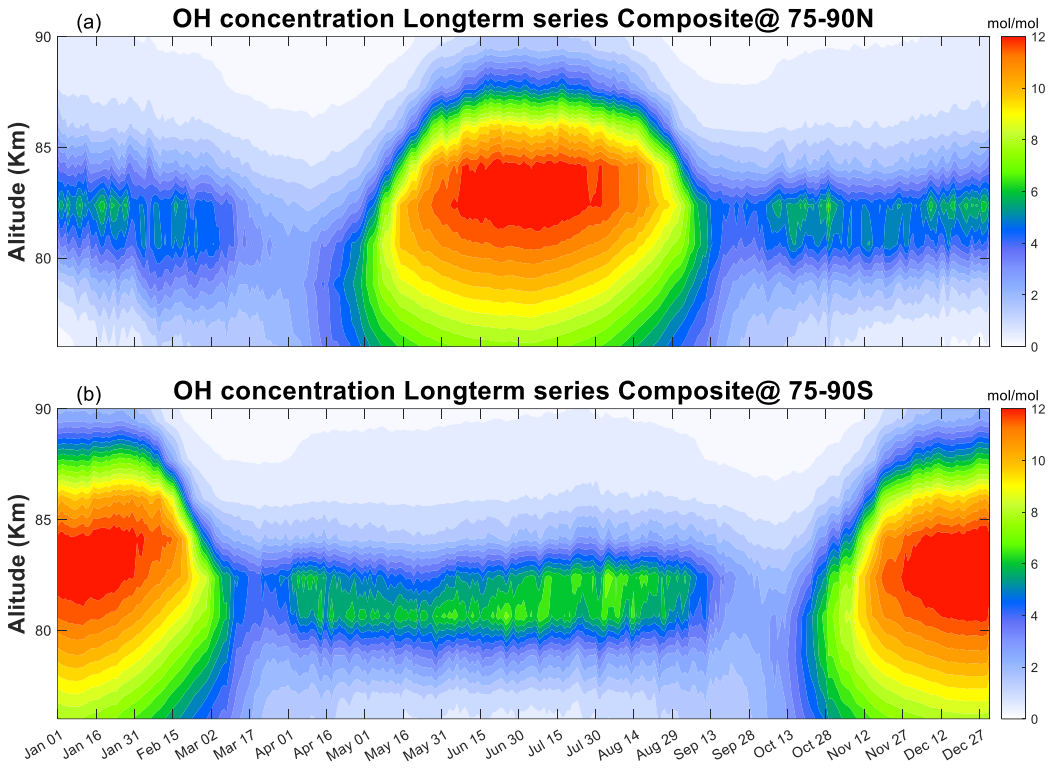

346

347 **Figure 3. Temporal evolution of OH concentration (in units of 10^{-9}) in the polar**
348 **region, with the Northern Hemisphere in the top panel and the Southern**
349 **Hemisphere in the bottom panel.**

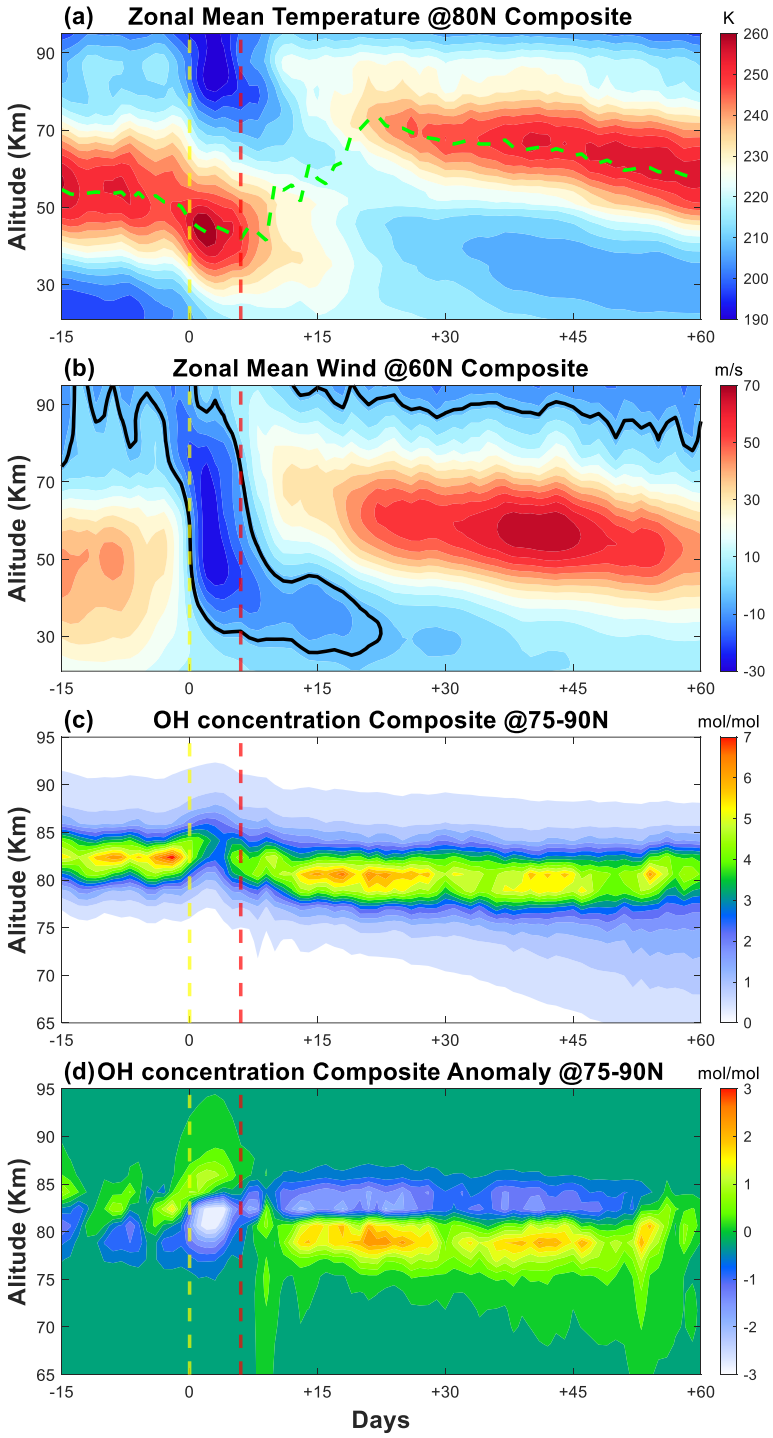

Figure 4. Time-altitude cross-section of composite zonal mean (a) temperature, (b) zonal wind, (c) OH concentration (in units of 10^{-9}), and (d) OH concentration anomaly. On the abscissa, time is relative to the ES-SSW onset (Day 0). Vertical dashed yellow and red lines are the onset of the stratosphere warming stage and elevated stratopause stage, respectively. The dashed green line is the stratopause height, while the black solid contour in (b) denotes the zero-wind line.

Figure 4 illustrates the composite evolution of zonal mean temperature, zonal mean wind, OH concentration, and ~~anomaly~~ OH concentration~~–~~ anomaly (Anomaly derived from original OH concentration minus background average) as functions of altitude and time. The background average of OH concentration is derived from the 20-year average from 2004 to 2023.~~as functions of altitude and time.~~ As depicted in Figures 4a and 4b, significant variations extend across nearly the entire altitude range. In the mesosphere, the zonal mean wind exhibits a rapid weakening of the eastward component around Day -8, then switches to westward after Day 0 with a minimum wind speed of around -27 m/s. Around Day 6, the eastward wind begins to intensify again, reaching a peak velocity exceeding 70 m/s near Day 40. Corresponding thermal changes accompany zonal wind reversal. At the onset of the ES-SSW event, the stratosphere undergoes rapid warming, leading to a sharp descent of the stratopause altitudes. As shown, until Day 3, the stratopause altitude reaches its lowest altitude of ~43.5 km, coinciding with the peak westward wind. The maximum temperature and wind speed are over 260 K and -27 m/s, respectively. After Day 6, as the eastward wind begins to strengthen, a newly formed stratopause emerges near 80 km.

The composite variabilities of OH concentrations and ~~anomaly~~ OH concentrations anomaly associated with ES-SSW events are examined, as shown in Figures 4c and 4d. Here, the composite results represent the mean structure aligning the temporal series of individual ES-SSW events. Figure 4c illustrates the temporal evolution of OH concentration. Prior to the onset of SSW, the peak of OH concentration exhibits a value of ~7.4×10^{-9} mol/mol, with a peak height near 82.4 km. During the stratosphere warming phase, the peak of OH concentration decreases to 2.9×10^{-9} mol/mol, while in the elevated stratopause phase, it increases to ~6.8×10^{-9} mol/mol. In addition, the peak height of OH concentration rises by ~3.5 km reaching ~85.9 km during the warming phase, before descending by ~2 km to ~80.6 km during the elevated stratopause phase. This temporal evolution is consistent with that in 2009 shown in Figure 1. Winick et al. (2009) proposed that the anomalous characteristics of the OH layer may be associated with changes in the atomic oxygen concentration and temperature in the mesosphere, which is driven by the modification of polar circulation induced by ES-SSW events.

Similarly, the temporal evolutions are depicted in Figure 4d, which represents the

variability of ~~anomaly~~ OH concentration~~–~~ anomaly~~(Anomaly = OH concentration – background average)~~. ~~The background averages of OH concentration are derived from the average of all aligned years from 2004 to 2023.~~ As shown, during the stratosphere warming phase, the peak height of ~~anomaly~~ OH concentration anomaly occurs at 85.9 km with a maximum of ~1.3×10^{-9} mol/mol. These situations in the elevated stratopause phase are significantly different. Compared to the stratosphere warming phase, the peak of ~~anomaly~~ OH concentration anomaly doubles, reaching a maximum of ~2.6×10^{-9} mol/mol, while its peak height significantly decreases to 78.8 km. These phenomena again demonstrate the consistency between OH concentration enhancements/depletions and peak height descent/ascent, a relationship previously documented in J. R. Winick.

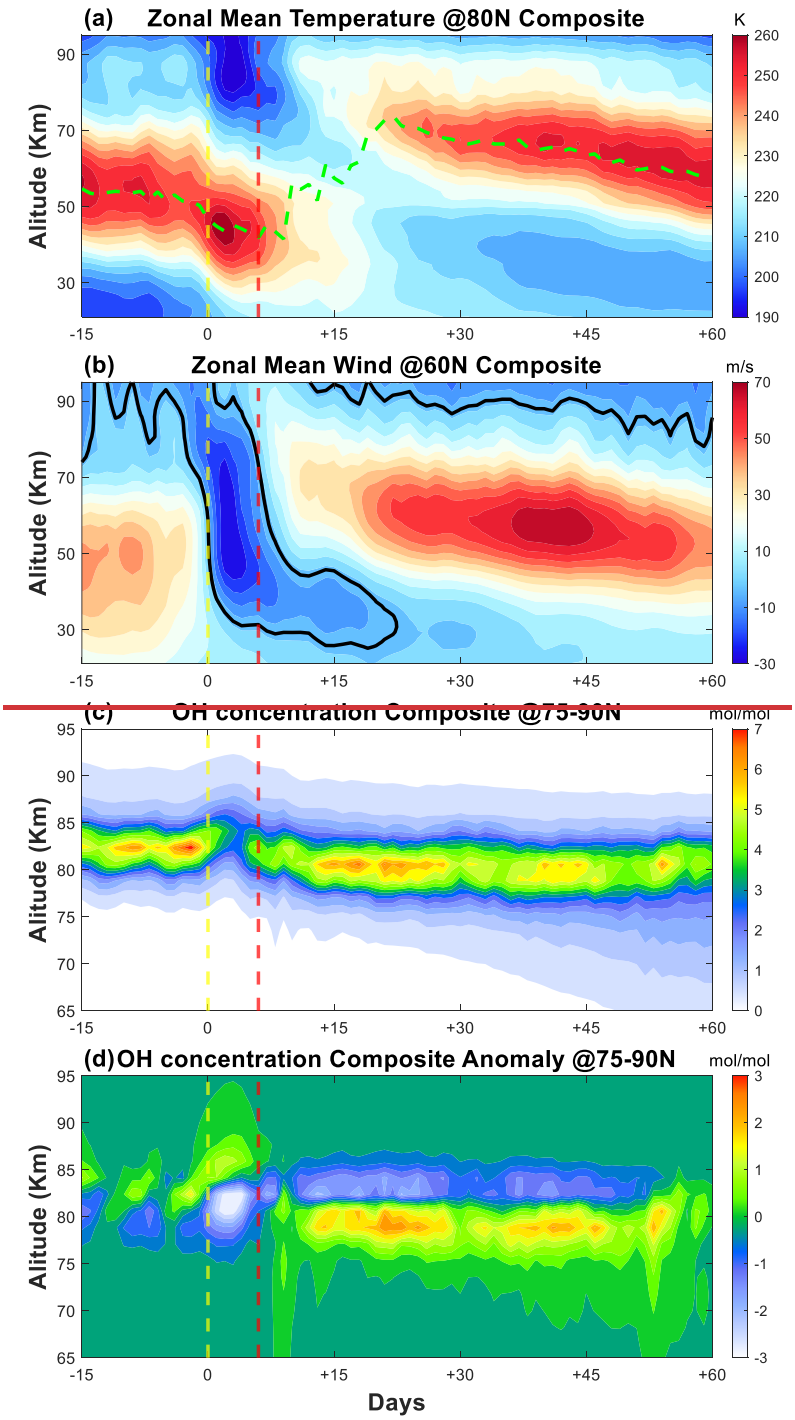

~~**Figure 4. Time-altitude cross-section of composite zonal mean (a) temperature, (b) zonal wind, (c) OH concentration (in units of 10^{-9}), and (d) anomaly OH concentration. On the abscissa, time is relative to the ES-SSW onset (Day 0). Vertical dashed yellow and red lines are the onset of the stratosphere warming stage and elevated stratopause stage, respectively. The dashed green line is the stratopause height, while the black solid contour in (b) denotes the zero-wind line.**~~

4. Discussion

4.1 Temporal variation

During the ES-SSW period, changes in atmospheric circulation lead to a strong descent/ascent motion of air at high latitudes. This dynamic change leads to subsequent increased/decreased atomic oxygen penetrating the mesopause. Within the mesospheric region, OH* is primarily produced through the reaction between ozone (O_3) and atomic hydrogen (H) (Marsh et al., 2006), as described by this equation:

$$O_3 + H \xrightarrow{k_1} OH^* + O_2 \quad (1)$$

According to Equation 1, the reaction rate coefficient k_1 increases with temperature, thereby enhancing the efficiency of OH* production. Ozone is formed through the reaction of atomic oxygen and molecular oxygen, as expressed in the equation:

$$O + O_2 + M \rightarrow O_3 + M \quad (2)$$

Notably, this process, $O + O_3 \rightarrow O_2 + O_2$, also contributes to ozone destruction alongside OH* production. However, below ~95 km, ozone loss due to its reaction with atomic hydrogen significantly exceeds that caused by atomic oxygen by several orders of magnitude (Xu et al., 2010). In addition, ozone may be treated as being in a steady state under nighttime conditions (i.e., polar winter), implying that the production of OH is proportional to atomic oxygen (Gao et al., 2011). This relationship indicates that the temporal evolution of OH concentration is strongly coupled with variations in atomic oxygen abundance and temperature in the mesopause.

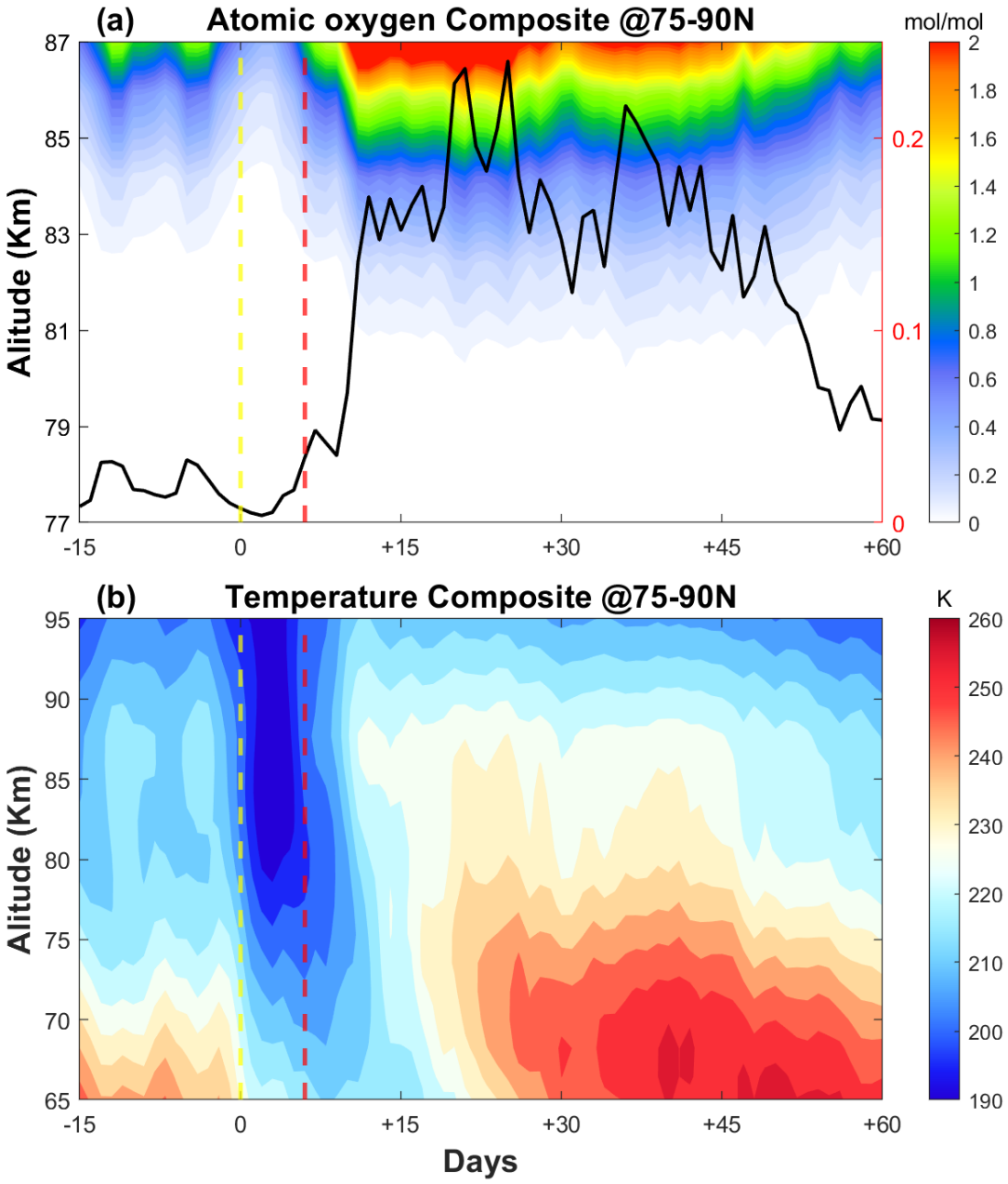

427

428 **Figure 5. Same as Figure 4, but for (a) atomic oxygen (in units of 10^{-3}) and (b)**
429 **temperature. The solid black line in (a) represents the temporal evolution of**
430 **atomic oxygen at 82 km.**

431 Figure 5 presents the composite variations in atomic oxygen (Figure 5a) and
432 temperature (Figure 5b) over high latitudes (75°-90°N). In Figure 5a, the solid black
433 line illustrates the temporal evolution of atomic oxygen concentration at 82 km. The
434 atomic oxygen concentration increases with altitude in the mesopause. Since the atomic
435 oxygen concentration is relatively low at this level, the line plot is included to clearly

highlight its variation throughout the event. The temporal variations of OH (Figure 4c), atomic oxygen (Figure 5a), and temperature (Figure 5b) in the mesopause region exhibit a nearly synchronous evolution. During the stratosphere warming phase, the atomic oxygen concentration experiences a significant decline, with a minimum value of ~0.005×10^{-3} mol/mol at 82 km, as indicated by the solid black line. Then, the atomic oxygen peak concentration remarkably increases, reaching a peak value of ~0.24×10^{-3} mol/mol, which is substantially higher than the normal stage. Figure 5b displays the composite temperature variation, which closely corresponds to the evolution of atomic oxygen. The temperature minimum reaches its minimum (~190 K) during the stratosphere warming stage and peaks at ~260 K in the elevated stratopause stage.

Figure 6 shows the ~~relative~~ temporal evolution ~~of the vertical component~~ of the residual circulation (~~w^*~~ $v^* = \bar{v} - \rho^{-1}(\rho\frac{\overline{v'\theta'}}{\bar{\theta}_z})_z$; $w^* = \bar{w} + (a\cos\varphi)^{-1}(\cos\varphi\frac{\overline{v'\theta'}}{\bar{\theta}_z})_\varphi$), where w^* and v^* denote~~and~~ the vertical and meridional ~~component~~ components of the residual circulation, respectively ~~(v^* ; $v^* = \bar{v} - \rho^{-1}(\rho\frac{\overline{v'\theta'}}{\bar{\theta}_z})_z$)~~. During the stratosphere warming phase, a strong downwelling (negative w^*) develops in the stratosphere with a value of -1 cm/s, denoting enhanced adiabatic heating. Meanwhile, an anomalous upwelling (positive w^*) emerges above ~70 km in the mesosphere, peaking at ~1.4 cm/s at ~77 km, suggesting a weakening or even reversal of the climatological downward branch of the residual circulation over the winter polar cap (e.g., Gao et al., 2010; Limpasuvan et al., 2016). These vertical circulation anomalies directly modulate the mesospheric thermal structure: the upwelling leads to adiabatic cooling, consistent with the temperature decrease observed in Figure 4a, while the subsequent recovery of strong downwelling in the elevated stratopause phase (up to -2.5 cm/s) contributes to mesospheric warming. Additionally, the upwelling during the stratosphere warming phase lifts air with lower atomic oxygen concentrations into the mesopause, resulting in a significant depletion of atomic oxygen (Figure 5a). In contrast,

enhanced downwelling during the elevated stratosphere phase brings oxygen-rich air downward, increasing atomic oxygen concentration and thereby promoting OH production. During the stratosphere warming stage, an anomalous equatorward flow also emerges near the mesopause (Figure 6b), indicating a temporal reversal of the climatological poleward residual circulation. As the stratopause elevates, this meridional circulation returns to a poleward pattern. The reversal and recovery of meridional circulation could promote inter-latitudinal transport, potentially contributing to OH variations at lower latitudes, such as the equatorial region.

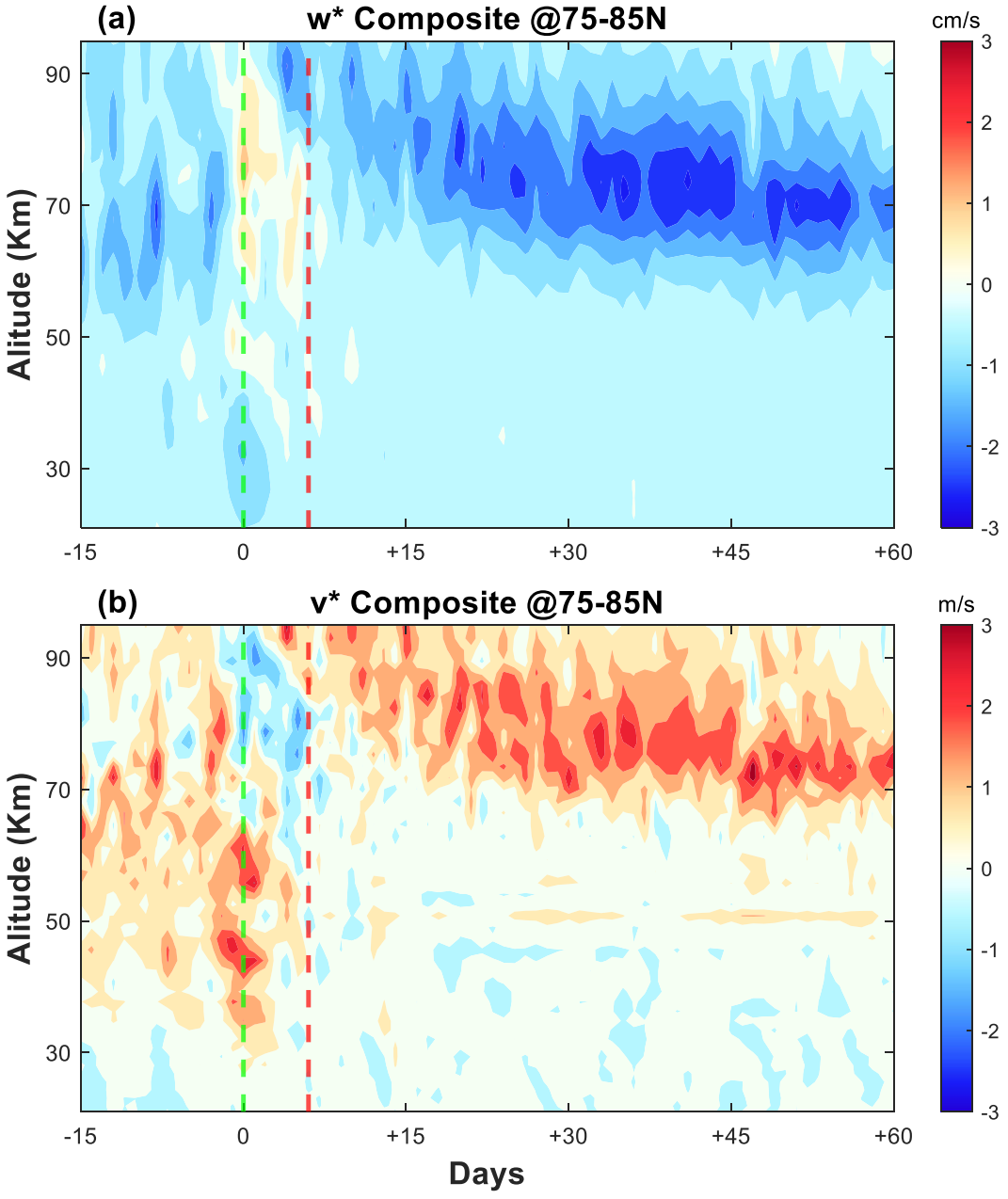

Figure 6. Same as Figure 4, but for (a) w^* and (b) v^*.

4.2 Spatial distribution

As shown in the preceding figures, the most prominent variations in OH concentration associated with ES-SSW event occur primarily within the first 30 days following the SSW onset, during which OH, atomic oxygen, temperature, and w^* exhibit substantial perturbations. To further investigate the meridional structure of these responses, the relative variations of these parameters are analyzed across three distinct stages: Stage 1 (Day -10 to Day 0), Stage 2 (Day 0 to Day 5), and Stage 3 (Day 6 to Day 26). Figures 7-9 present the corresponding spatial distributions of each parameter during these stages. The relative variation is derived as follows:

$$\text{Reletive variation} = \frac{X_{(i)} - \overline{X}}{\overline{X}} \times 100\% \quad (3)$$

in which $X_{(i)}$ represents the variable (OH, atomic oxygen, and temperature) for each ES-SSW event, and $\overline{X}$ stands for the background average obtained by averaging the same calendar dates over 2004–2023.

Figure 7 illustrates the ES-SSW-related parameters as functions of latitude and altitude in Stage 1. The spatial structure of OH concentration in the polar mesosphere is depicted in Figure 7a. A local maximum appears near ~83 km with an enhancement of 10% relative to the background average, whereas below 80 km, OH concentration exhibits a marked decrease, reaching a minimum of -35.7%. Figure 7b presents the situation of the atomic oxygen, which displays notable differences from OH. For instance, the enhancement shifts downward, with a peak of 25.4% located near ~75 km, while the minimum atomic oxygen concentration reaches -46.3% at ~81 km in the polar region. The corresponding temperature distribution (Figure 7c) reveals a warming in the polar stratosphere and cooling in the polar mesosphere with the magnitudes of approximately 3% and -3%, respectively. Figure 7d shows the~~–~~ w^* anomaly, which increases slightly to ~0.4 cm/s between ~65 and 83 km at high latitude. Simultaneously, the polar v^* anomaly~~meridional circulation~~, as indicated by the white arrows, shifts equatorward in the mesosphere. ~~Prior to the SSW onset~~In climatology, the circulation pattern is characterized by a pole-to-pole circulation from the summer hemisphere toward the winter hemisphere. Notably, slight variations in these parameters can be

detected even prior to the onset of the ES-SSW event. This early-stage response may be attributed to the fact that ES-SSW perturbances tend to emerge in the mesosphere several days before becoming evident in the stratosphere (Gao et al., 2011), as also reflected by the temperature variations in Figure 4a.

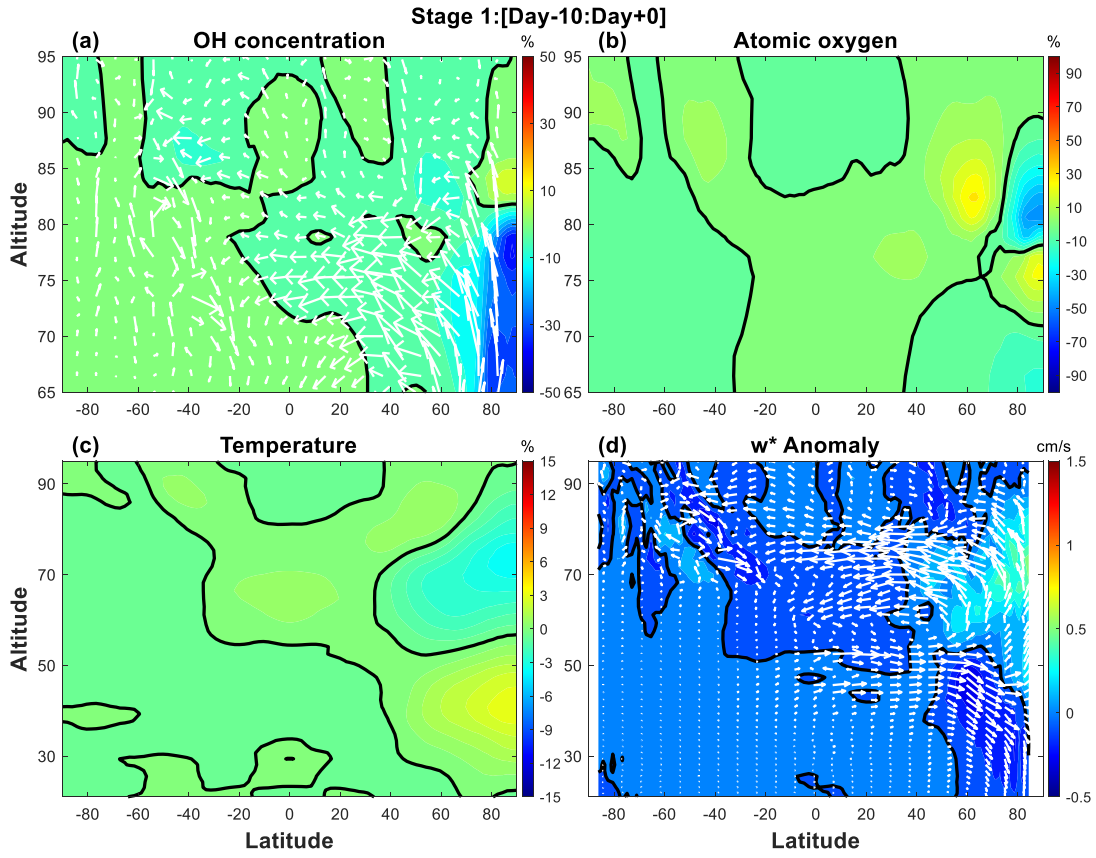

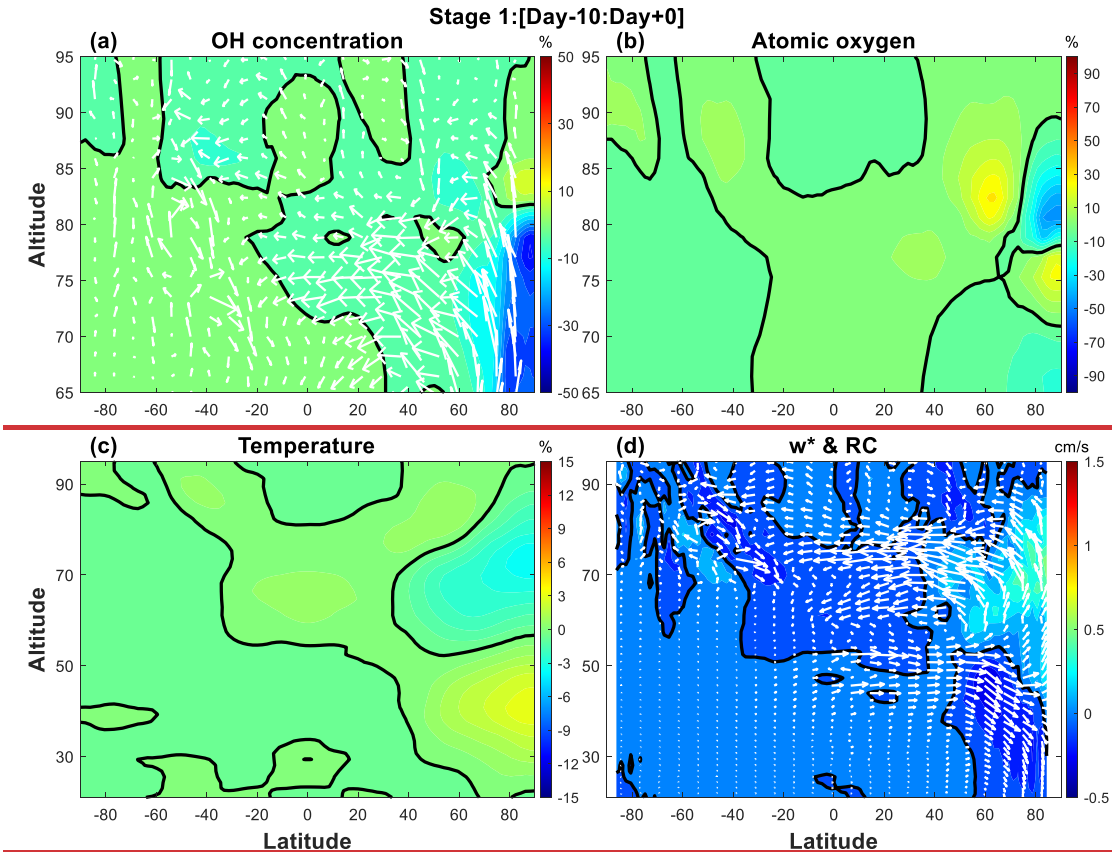

Figure 7. Latitude-altitude cross-sections of composite relative variation in (a) OH, (b) atomic oxygen, and (c) temperature, and composite ~~absolute variation~~anomaly in (d) w^* during Day -10 to Day 0 (Stage 1). The zero contour is denoted by a bold solid black line, and white arrows in (a) and (d) represent the residual circulation anomaly.

Figure 8 illustrates the latitude-altitude structure of various elements in Stage 2, which exhibit significant responses to ES-SSW events. Compared to Stage 1, the OH concentration (Figure 8a) in the polar region displays a marked enhancement with a maximum increase of ~75.9% relative to the background average occurring at ~85.9 km. Conversely, the minimum OH concentration reaches a pronounced decrease with an amplitude of -63.5% at ~78.8 km. The variations in atomic oxygen (in Figure 8b) are even more pronounced concerning Stage 2 over the latitudinal range of 75°-90°N, with a minimum reduction to -90.8% and a maximum increase to ~48.3% with respect to the background average. The temperature distribution in Figure 8c also reveals a noticeable response to the ES-SSW events, with a positive anomaly of 13.9% centered near 32 km and a negative anomaly of -11% around 84 km in the polar region. Figure

8d shows the spatial structure of– *w** anomaly in Stage 2. Compared to Stage 1, the magnitude of— *w** anomaly in the polar mesosphere increases significantly, exceeding 1.78 cm/s between ~64.6 km and ~78.8 km. These vertical structures are consistent with the findings of Dyrland et al. (2010) that associated OH airglow temperature perturbations with neutral atmospheric dynamics during the anomalous 2003-2004 winter. Their study also noted altitude-dependent evolution of the polar vortex.

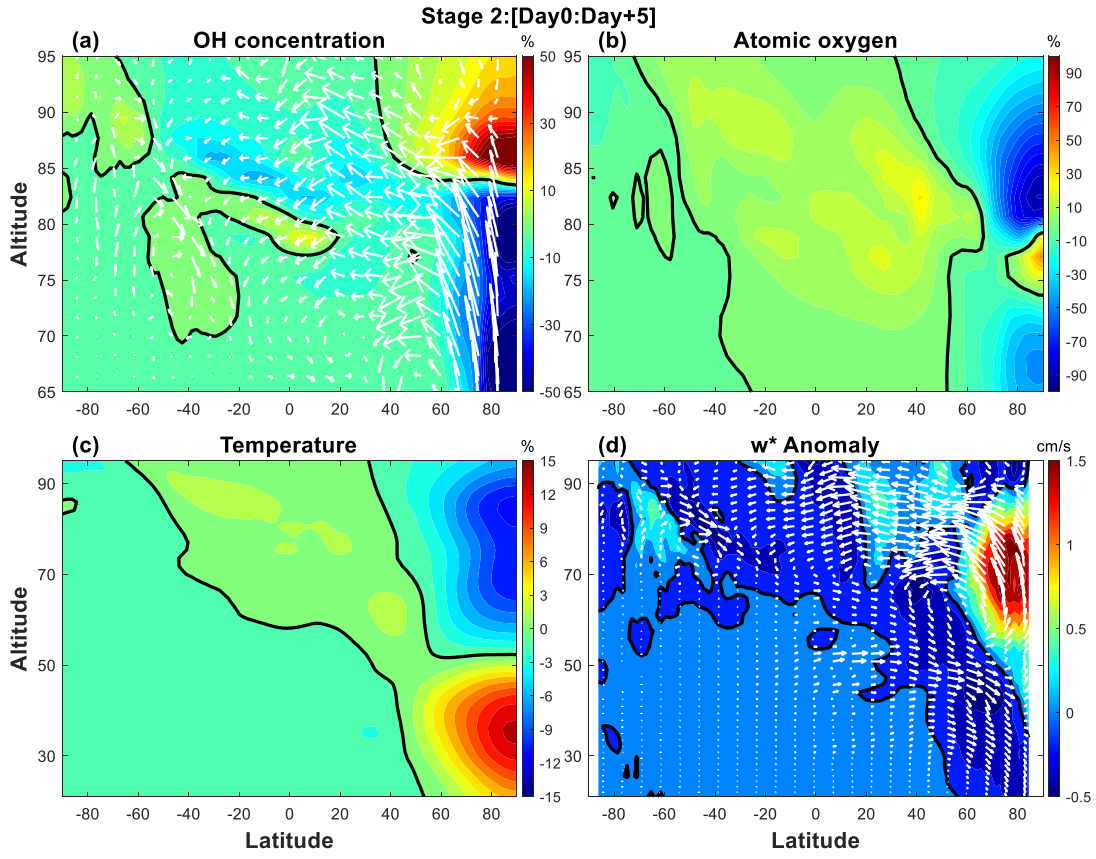

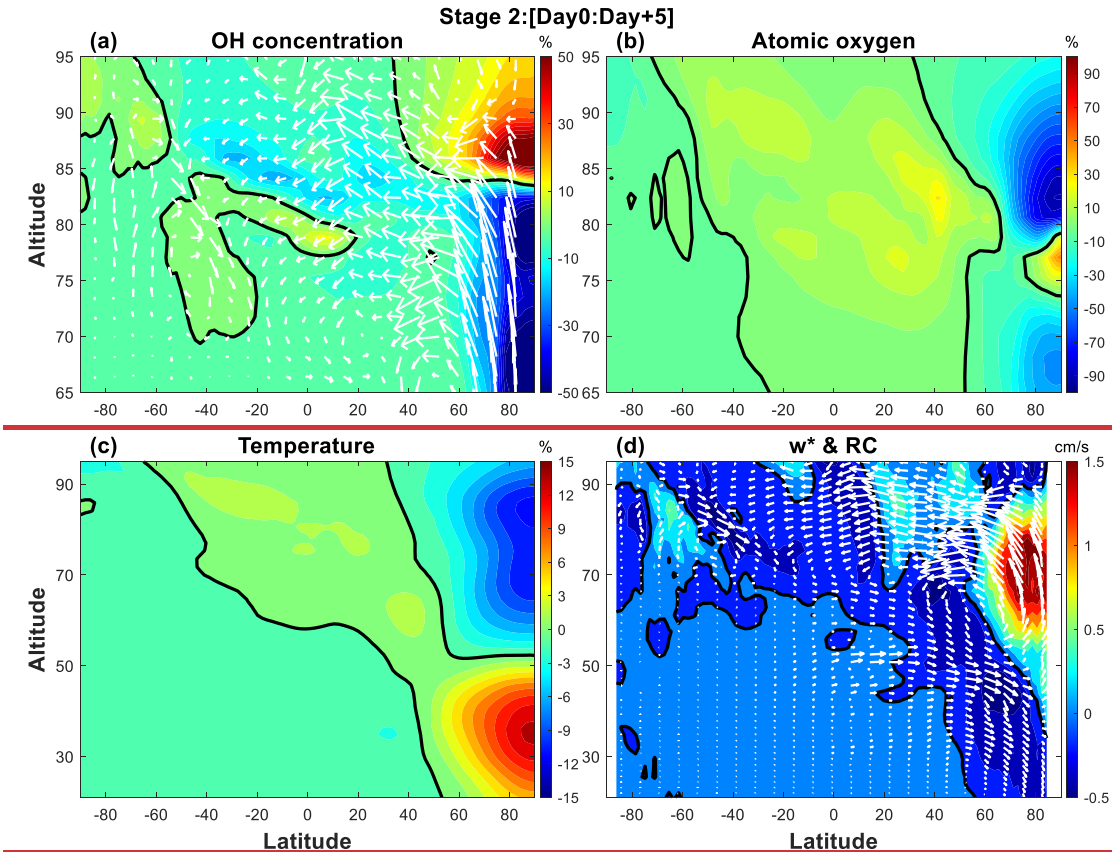

Figure 8. Same as Figure 7, but for Day 0 to Day 5 (Stage 2).

In the present work, the ~~intensified upward residual circulation~~positive *w** anomaly at high northern latitudes is clearly observed, as indicated by the white arrows in Figure 8d. This upward motion turns equatorward in the upper mesosphere, forming a distinct pole-to-equator branch of the mesospheric circulation. Simultaneously, below ~50 km, the poleward circulation exhibits a downward motion at the middle and high latitudes. The high-latitude downward circulation below ~50 km and upward circulation above ~50 km result in corresponding stratospheric warming and mesospheric cooling during the SSW period (as also shown in Figure 4a), respectively. Moreover, the upward transport of oxygen-poor air to higher latitudes, facilitated by ~~enhanced~~ positive *w** anomaly~~residual circulation~~, results in a significant reduction in atomic oxygen concentrations. As a consequence, the peak height of OH layer shifts upward, accompanied by a notable decrease in its peak concentration.

In addition, notable variations in OH concentration are also evident in the equatorial mesosphere region during Stage 2. Relative to the background average, a secondary OH peak appears at ~78.8 km with an amplitude of ~13.6%, while a local

minimum of approximately -16.9% occurs at a higher altitude of ~82.4 km. Concurrently, both atomic oxygen and temperature exhibit modest enhancements in the equatorial mesosphere, with amplitudes of ~16% and ~1.5%, respectively. The observed temperature response in the equatorial region is consistent with that reported by Gu et al. (2021) in their analysis of the 2009 major SSW event (see their Figure 2e), which documented the middle atmospheric circulation response to SSW. However, the underlying dynamical and chemical mechanisms responsible for these compositional changes in the equatorial region remain unclear and warrant further investigation.

Figure 9 depicts the spatial distribution of multiple parameters during Stage 3, corresponding to Day 6 through Day 26 following the onset of the SSW. Compared to the preceding stages, the polar OH concentration structure undergoes a distinct reversal in vertical pattern. Specifically, the OH peak descends to ~78.8 km and intensifies to ~59.5%, while the minimum shifts to a higher altitude (~84.2 km) and weakens to negative 37.7%. As shown in Figure 9b, the atomic oxygen concentration exhibits a pronounced enhancement, with its peak occurring at ~82.4 km and exceeding 137.3% compared to the climatological average at high latitudes. The temperature field (Figure 9c) displays a bifurcated structure, with a dominant warming centered around ~28 km with an amplitude of ~7.9% and a secondary weaker warming near the MLT region with a lower amplitude of ~3.7%. The vertical structure of the residual circulation anomaly (Figure 9d) also changes noticeably. The peak of w^* anomaly shifts downward to ~57 km with a reduced amplitude (~0.51 cm/s) in the polar region compared to earlier stages. As the mesospheric wind begins to eastward, the residual circulation anomaly transitions to a pole-to-pole pattern from the summer to winter hemisphere, and then descends vertically above ~70 km in the polar region. ~~This~~ The negative w^*~~downward motion~~ facilitates the downward transport of oxygen-rich air into the polar mesopause region and warming around 80 km. Consequently, the OH concentration peak increases in magnitude while its altitude decreases. In the equatorial region, the OH distribution in Stage 3 resembles that in Stage 2 but with reduced amplitude. The sustained presence of these anomalies may be attributed to continued enhancements in both atomic oxygen abundance and temperature in the equatorial region.

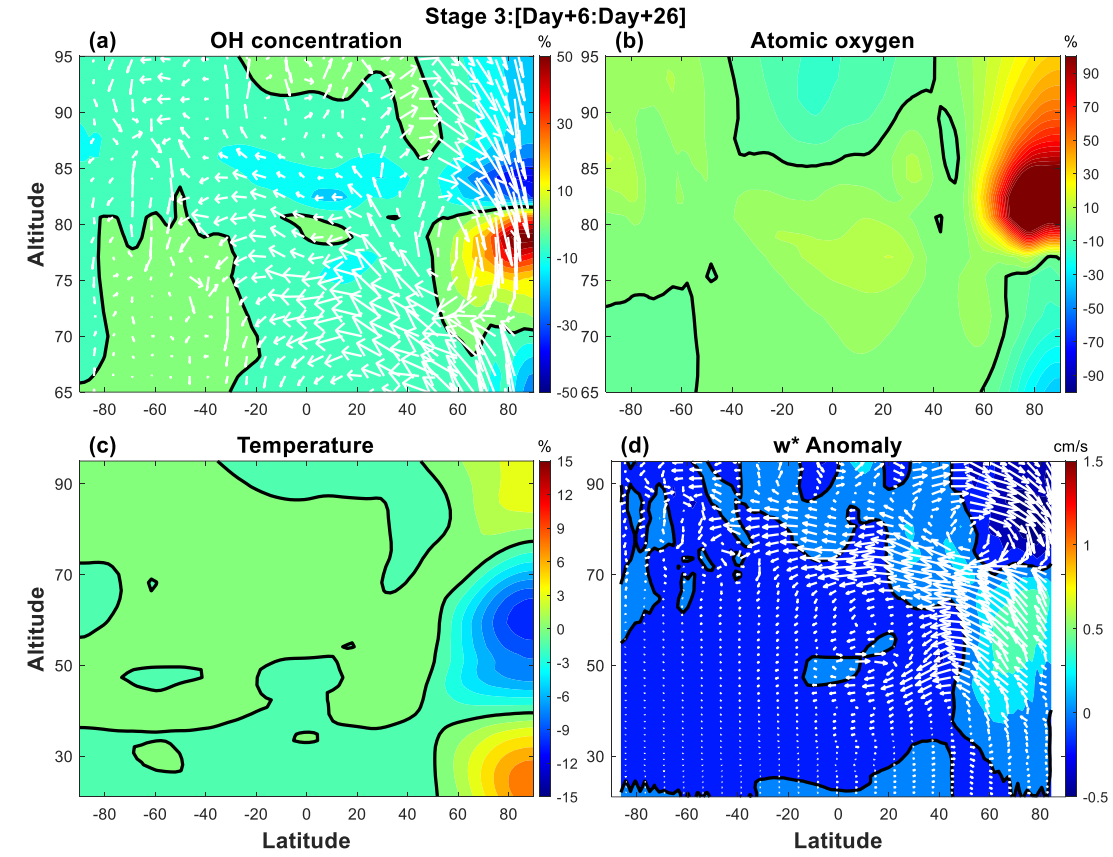

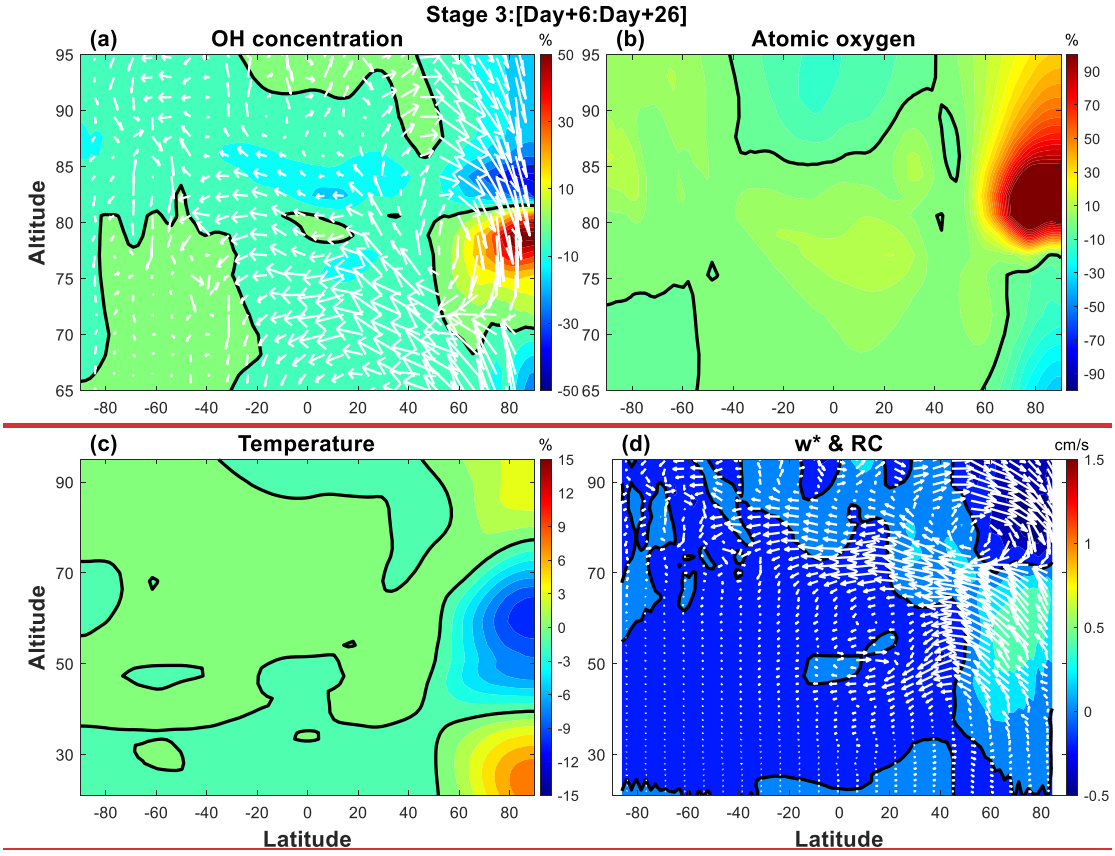

Figure 9. Same as Figure 7, but for Day 6 to Day 26 (Stage 3).

4.3 Potential mechanism

583 During SSW events, the reversal/deceleration of the stratospheric winter eastward
584 wind due to planetary wave breaking allows more eastward-propagating GWs to
585 penetrate into higher altitudes, enhancing upward and equatorward motion in the
586 mesosphere. This altered circulation results in mesospheric cooling (Limpasuvan et al.,
587 2012; Lukianova et al., 2015; Gu et al., 2021). The mesospheric OH layer variability
588 may be dominantly controlled by changes in GWs during the ES-SSW events.
589 Figure 10 presents the temporal evolution of zonal wind tendency due to total
590 gravity wave drag (GWD) and zonal wind tendency due to orographic gravity wave
591 drag over the latitudes of 40°-80°N. Under the quiet conditions, westward GWs drag in
592 the mesosphere ~~sustains~~ sustain the polar circulation downwelling. As planetary wave
593 activity intensifies, the weakening/reversal of the eastward jet starts in the mesosphere
594 and progresses to the stratosphere (Yang et al., 2024; Liu and Roble, 2005), with
595 mesospheric changes preceding the stratospheric response by several days in Figure 4b
596 (Gao et al., 2011; Coy et al., 2011; Kurihara et al., 2010; Azeem et al., 2005). Alteration
597 of the wave transmission conditions enables eastward-propagating GWs to penetrate
598 the mesosphere resulting in enhanced eastward GWD that modulates the mesospheric
599 circulation (Figure 6) and induces a slight response in the polar OH layer (Figure 7a).

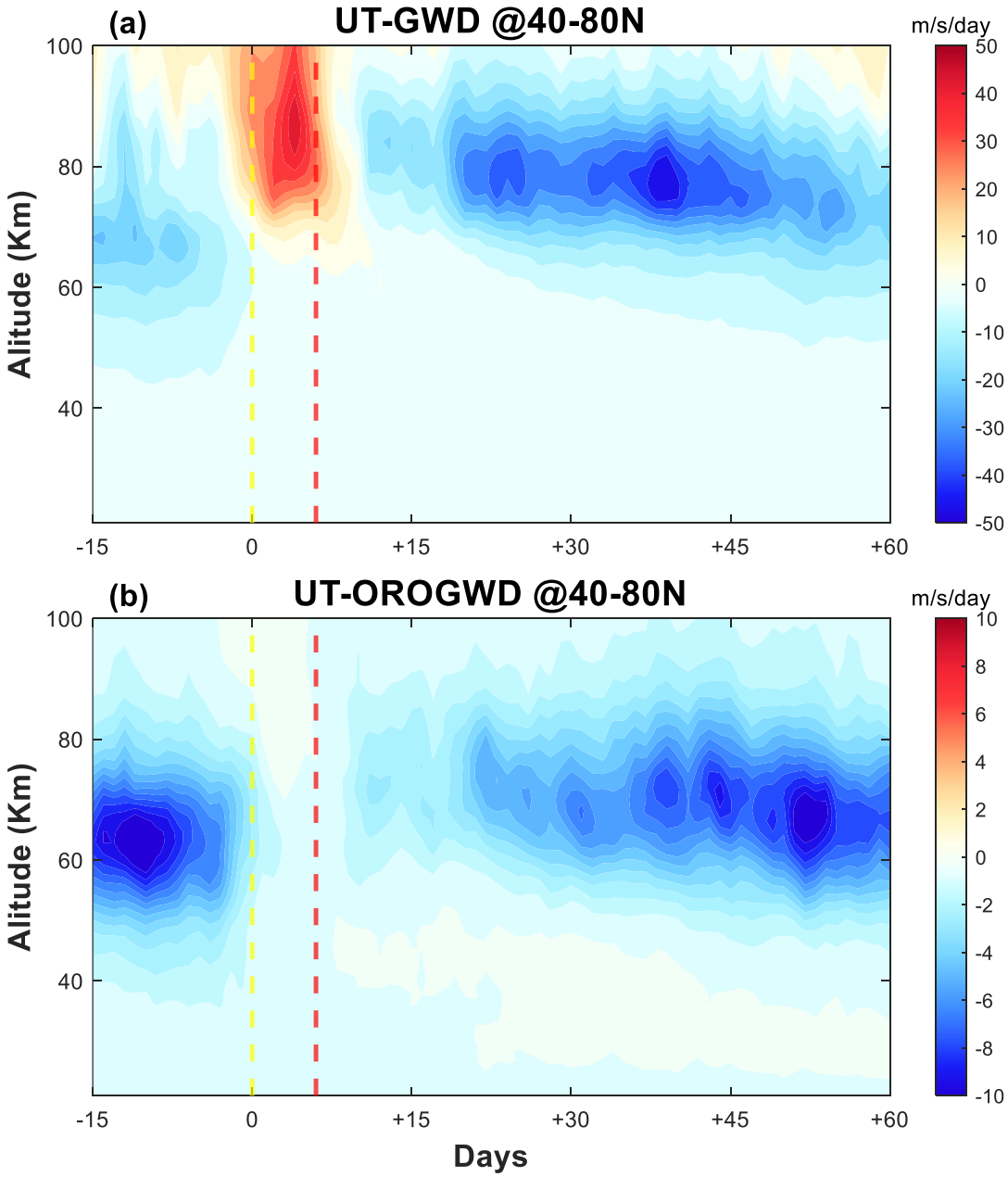

Figure 10. Time-altitude cross-section of SD-WACCM-X composite zonal mean (a) zonal wind tendency due to total gravity wave drag (UT-GWD) and (b) zonal wind tendency due to orographic gravity wave drag (UT-OROGWD).

Following the stratosphere warming phase, a reversal of the zonal-mean wind from eastward to westward in the polar stratosphere and mesosphere is evident in Figure 4b. The stratospheric westward wind filters out westward phase speed components of GWs and facilitates the upward propagation of eastward-propagating GWs into the mesosphere, which results in anomalously eastward GWs exerting strong positive zonal wind tendency as shown in Figure 10a, peaking in the mesosphere around Day 4 with

its maximum of 46.2 m/s/day. Enhanced eastward GWs forcing induces equatorward flow in the mesopause region and enhances the upward residual circulation extending from the stratosphere to the mesosphere at northern high latitudes, which can be seen vertical component and meridional component of residual circulation in Figures 6 and 8d. This upward residual circulation transports oxygen-poor air upward, given that atomic oxygen concentration increases with altitude (seen in Figure 5a), leading to a reduction in atomic oxygen abundance in the upper atmosphere. As a result, the peak OH concentration exhibits a substantial decrease, while its corresponding peak altitude undergoes a pronounced upward shift.

During the elevated stratopause phase, the thermal relaxation rate in the upper mesosphere and lower stratosphere is approximately two to three times that of the lower stratosphere (Wehrbein and Leovy, 1982; Chandran et al., 2014), promoting the rapid recovery of the polar eastward zonal wind (Hitchman et al., 1989). Consistent with the initial response to the disturbance, the recovery of eastward zonal winds first appears in the mesosphere and then progressively propagates downward into the stratosphere. The GWs with westward phase speeds are again able to propagate into the mesosphere and subsequently dissipate, inducing a pronounced negative zonal wind tendency with a peak value reaching ~-45 m/s/day exceeding the climatological average. Enhanced GW breaking at higher latitudes within the MLT region drives an intensified poleward and downward branch of the residual circulation, leading to the reformation of elevated stratopause at high latitudes, as shown in Figure 4a (Chandran et al., 2014). Compared to quiet conditions, where such circulation is largely confined below 50 km, the poleward and downward flow extends above 70 km in the elevated stratopause phase. This pronounced downward motion promotes the descent of dry mesospheric air (Orsolini et al., 2010), which causes an exceptionally strong vertical transport of atomic oxygen into the mesopause region. Consequently, the OH concentration returns toward the climatological level, with the peak of OH layer occurring at a lower altitude.

Generally, GWs can be categorized into orographic and non-orographic components (Gilli et al., 2020; Richter et al., 2010). As shown in Figure 10b, the momentum deposition induced by orographic GWs is primarily confined to the altitude range of 40~80 km with values ranging from -10.5 to 0.5 m/s/day. During the

stratosphere warming phase, orographic GWs are largely filtered and inhibited from upward propagation, leading to a notable reduction of their drag contribution (Liu et al., 2019). In the elevated stratopause phase, the zonal wind tendency associated with orographic GWD shows a different vertical structure compared to that associated with total GWD (see Figure 10a), particularly exhibiting a less significant enhancement at higher altitudes. It is demonstrated that orographically generated GWs play a secondary role in the overall momentum budget relative to non-orographic GWs. Non-orographic GWs, which are parameterized mainly from frontogenesis and convection sources (Holt et al., 2017), dominate the momentum deposition in the mesospheric polar region during ES-SSW events. The contribution from convective GWs is comparatively negligible, while frontogenetical generated GWs emerge as the primary source of GWs drag (Limpasuvan et al., 2012; Limpasuvan et al., 2016). Given the dominant role of frontogenesis GWs in driving mesospheric dynamics during ES-SSW events, it is suggested that the variability observed in the OH layer is predominantly modulated by gravity wave activity associated with frontogenesis.

5 Conclusions

In this paper, the responses of the peak concentration and peak height changes in the polar OH layer to ES-SSW events in the mesosphere are investigated based on SD-WACCM-X simulations. By compositing ten ES-SSW events from 2004 to 2023, distinct variations in OH layer structure associated with different phases of these events are revealed. The results demonstrate that the anomalous behaviors of the OH concentrations are closely synchronous with changes in mesospheric temperature, atomic oxygen concentrations, and the vertical component of the residual circulation in the MLT region. GWs play a pivotal role by altering the vertical motion of circulation in the MLT region, which modulates the zonal wind and temperature fields. The enhanced downward/upward motion driven by GWs leads to mesospheric warming/cooling and an increase/decrease in atomic oxygen, which facilitates an increase/decrease in OH concentration.

The impact of ES-SSW extends well from the polar to the equator, strongly altering the zonal-mean zonal wind, temperature, and atomic oxygen distribution.

However, the response of the mesopause OH layer in the equatorial region to ES-SSW is unclear. Our study enhances the understanding of OH layer responses to stratospheric perturbations and provides new insights into vertical coupling processes in the middle and upper atmosphere. Future research should focus on quantifying the relative contributions of these factors and assessing their implications for long-term atmospheric dynamics and chemistry.

Data availability.

WACCM-X is an open-source software with source code publicly available at https://escomp.github.io/CESM/release-cesm2/downloading_cesm.html#downloading-the-code-and-scripts. The atmospheric forcing data, which are regridded from the MERRA-2 data set and used to run WACCM-X, can be downloaded at https://rda.ucar.edu/datasets/ds313.3/?hash=access. The SABER data employed in this study are available at https://saber.gats-inc.com/data.php. For access to the SD-WACCM-X simulation data, please contact the corresponding authors: Sheng-yang Gu (gushengyang@whu.edu.cn) or Yusong Qin (qinyusong@whu.edu.cn).

Author contribution. Conceptualization and investigation were conducted by Jin Hu. Formal analysis and visualization were performed by Jin Hu with guidance and supervision from Sheng-yang Gu and Yusong Qin. Data curation for SD-WACCM-X was carried out by Yuxuan Liu. All authors contributed to the discussion of results and the revision of the manuscript.

Competing interests. The contact author has declared that none of the authors has any competing interests.

Acknowledgments. The authors acknowledge the National Center for Atmospheric Research (NCAR) for providing the SD-WACCM-X model simulations and NASA for supplying the MERRA-2 reanalysis data. We are also grateful to the SABER team for providing the data used in this paper.

Financial support. This research was supported by the National Natural Science Foundation of China (Grant Numbers 42374195 and 42404168), the fellowship of China National Postdoctoral Program for Innovative Talents (Grant Number BX20230273), the Hubei Provincial Natural Science Foundation of China (Grant Number 2024AFB097), and the Postdoctor Project of Hubei Province (Grant Number 2024HBBHCXA054).

Reference

Azeem, S. M. I., Talaat, E. R., Sivjee, G. G., Liu, H. L., and Roble, R. G.: Observational study of the 4-day wave in the mesosphere preceding the sudden stratospheric warming events during 1995 and 2002, Geophysical Research Letters, 32, https://doi.org/10.1029/2005gl023393, 2005.

Baldwin, M. P. and Dunkerton, T. J.: Stratospheric harbingers of anomalous weather regimes, Science, 294, 581–584, https://doi.org/10.1126/science.1063315, 2001.

Bolaji, O. S., Oyeyemi, E. O., Owolabi, O. P., Yamazaki, Y., Rabiu, A. B., Fujimoto, D. O. A., Amory-Mazaudier, C., Seemala, G. K., Yoshikawa, A., and Onanuga, O. K.: Solar quiet current response in the African sector due to a 2009 sudden stratospheric warming event, Journal of Geophysical Research-Space Physics, 121, 8055–8065, https://doi.org/10.1002/2016ja022857, 2016.

Brakebusch, M., Randall, C. E., Kinnison, D. E., Tilmes, S., Santee, M. L., and Manney, G. L.: Evaluation of Whole Atmosphere Community Climate Model simulations of ozone during Arctic winter 2004-2005, Journal of Geophysical Research-Atmospheres, 118, 2673–2688, https://doi.org/10.1002/jgrd.50226, 2013.

Chandran, A., Collins, R. L., and Harvey, V. L.: Stratosphere-mesosphere coupling during stratospheric sudden warming events, Advances in Space Research, 53, 1265–1289, https://doi.org/10.1016/j.asr.2014.02.005, 2014.

Chandran, A., Collins, R. L., Garcia, R. R., Marsh, D. R., Harvey, V. L., Yue, J., and de la Torre, L.: A climatology of elevated stratopause events in the whole atmosphere community climate model, Journal of Geophysical Research-Atmospheres, 118,

734 1234–1246, https://doi.org/10.1002/jgrd.50123, 2013.
735 Charlton, A. J. and Polvani, L. M.: A new look at stratospheric sudden warmings. Part
736 I: Climatology and modeling benchmarks, Journal of Climate, 20, 449–469,
737 https://doi.org/10.1175/Jcli3996.1, 2007.
738 Chen, G., Wu, C., Zhang, S. D., Ning, B. Q., Huang, X. Q., Zhong, D. K., Qi, H., Wang,
739 J., and Huang, L.: Midlatitude ionospheric responses to the 2013 SSW under high
740 solar activity, Journal of Geophysical Research-Space Physics, 121, 790–803,
741 https://doi.org/10.1002/2015ja021980, 2016.
742 Coy, L., Eckermann, S. D., Hoppel, K. W., and Sassi, F.: Mesospheric Precursors to the
743 Major Stratospheric Sudden Warming of 2009: Validation and Dynamical
744 Attribution Using a Ground-to-Edge-of-Space Data Assimilation System, Journal
745 of Advances in Modeling Earth Systems, 3,
746 https://doi.org/10.1029/2011ms000067, 2011.
747 Damiani, A., Storini, M., Santee, M. L., and Wang, S.: Variability of the nighttime OH
748 layer and mesospheric ozone at high latitudes during northern winter: influence of
749 meteorology, Atmospheric Chemistry and Physics, 10, 10291–10303,
750 https://doi.org/10.5194/acp-10-10291-2010, 2010.
751 Danabasoglu, G., Lamarque, J. F., Bacmeister, J., Bailey, D. A., DuVivier, A. K.,
752 Edwards, J., Emmons, L. K., Fasullo, J., Garcia, R., Gettelman, A., Hannay, C.,
753 Holland, M. M., Large, W. G., Lauritzen, P. H., Lawrence, D. M., Lenaerts, J. T.
754 M., Lindsay, K., Lipscomb, W. H., Mills, M. J., Neale, R., Oleson, K. W., Otto-
755 Bliesner, B., Phillips, A. S., Sacks, W., Tilmes, S., van Kampenhout, L.,
756 Vertenstein, M., Bertini, A., Dennis, J., Deser, C., Fischer, C., Fox-Kemper, B.,
757 Kay, J. E., Kinnison, D., Kushner, P. J., Larson, V. E., Long, M. C., Mickelson, S.,
758 Moore, J. K., Nienhouse, E., Polvani, L., Rasch, P. J., and Strand, W. G.: The
759 Community Earth System Model Version 2 (CESM2), Journal of Advances in
760 Modeling Earth Systems, 12, https://doi.org/10.1029/2019MS001916, 2020.
761 de la Torre, L., Garcia, R., Barriopedro, D., and Chandran, A.: Climatology and
762 characteristics of stratospheric sudden warmings in the Whole Atmosphere
763 Community Climate Model, JOURNAL OF GEOPHYSICAL RESEARCH-
764 ATMOSPHERES, 117, https://doi.org/10.1029/2011JD016840, 2012.

765 de Wit, R. J., Hibbins, R. E., Espy, P. J., Orsolini, Y. J., Limpasuvan, V., and Kinnison,
766 D. E.: Observations of gravity wave forcing of the mesopause region during the
767 January 2013 major Sudden Stratospheric Warming, Geophysical Research Letters,
768 41, 4745–4752, https://doi.org/10.1002/2014gl060501, 2014.
769 Dyrland, M., Mulligan, F., Hall, C., Sigernes, F., Tsutsumi, M., and Deehr, C.: Response
770 of OH airglow temperatures to neutral air dynamics at 78°N, 16°E during the
771 anomalous 2003-2004 winter, JOURNAL OF GEOPHYSICAL RESEARCH-
772 ATMOSPHERES, 115, https://doi.org/10.1029/2009JD012726, 2010.
773 Gao, H., Xu, J. Y., and Chen, G. M.: The responses of the nightglow emissions observed
774 by the TIMED/SABER satellite to solar radiation, Journal of Geophysical
775 Research-Space Physics, 121, 1627–1642, https://doi.org/10.1002/2015ja021624,
776 2016.
777 Gao, H., Xu, J. Y., and Wu, Q. A.: Seasonal and QBO variations in the OH nightglow
778 emission observed by TIMED/SABER, Journal of Geophysical Research-Space
779 Physics, 115, https://doi.org/10.1029/2009ja014641, 2010.
780 Gao, H., Xu, J. Y., Ward, W., and Smith, A. K.: Temporal evolution of nightglow
781 emission responses to SSW events observed by TIMED/SABER, Journal of
782 Geophysical Research-Atmospheres, 116, https://doi.org/10.1029/2011jd015936,
783 2011.
784 Gettelman, A., Mills, M. J., Kinnison, D. E., Garcia, R. R., Smith, A. K., Marsh, D. R.,
785 Tilmes, S., Vitt, F., Bardeen, C. G., McInerny, J., Liu, H. L., Solomon, S. C.,
786 Polvani, L. M., Emmons, L. K., Lamarque, J. F., Richter, J. H., Glanville, A. S.,
787 Bacmeister, J. T., Phillips, A. S., Neale, R. B., Simpson, I. R., DuVivier, A. K.,
788 Hodzic, A., and Randel, W. J.: The Whole Atmosphere Community Climate Model
789 Version 6 (WACCM6), Journal of Geophysical Research-Atmospheres, 124,
790 12380–12403, https://doi.org/10.1029/2019jd030943, 2019.
791 Gilli, G., Forget, F., Spiga, A., Navarro, T., Millour, E., Montabone, L., Kleinböhl, A.,
792 Kass, D. M., McCleese, D. J., and Schofield, J. T.: Impact of Gravity Waves on
793 the Middle Atmosphere of Mars: A Non-Orographic Gravity Wave
794 Parameterization Based on Global Climate Modeling and MCS Observations,
795 Journal of Geophysical Research-Planets, 125,

https://doi.org/10.1029/2018JE005873, 2020.

Goncharenko, L., Chau, J. L., Condor, P., Cster, A., and Benkevitch, L.: Ionospheric effects of sudden stratospheric warming during moderate-to-high solar activity: Case study of January 2013, Geophysical Research Letters, 40, 4982–4986, https://doi.org/10.1002/grl.50980, 2013.

Grygalashvyly, M., Pogoreltsev, A. I., Andreyev, A. B., Smyshlyaev, S. P., and Sonnemann, G. R.: Semi-annual variation of excited hydroxyl emission at mid-latitudes, Annales Geophysicae, 39, 255–265, https://doi.org/10.5194/angeo-39-255-2021, 2021.

Gu, S. Y., Teng, C. K. M., Li, N., Jia, M. J., Li, G. Z., Xie, H. Y., Ding, Z. H., and Dou, X. K.: Multivariate Analysis on the Ionospheric Responses to Planetary Waves During the 2019 Antarctic SSW Event, Journal of Geophysical Research-Space Physics, 126, https://doi.org/10.1029/2020JA028588, 2021.

Harada, Y., Goto, A., Hasegawa, H., Fujikawa, N., Naoe, H., and Hirooka, T.: A Major Stratospheric Sudden Warming Event in January 2009, Journal of the Atmospheric Sciences, 67, 2052–2069, https://doi.org/10.1175/2009jas3320.1, 2010.

Harada, Y., Sato, K., Kinoshita, T., Yasui, R., Hirooka, T., and Naoe, H.: Diagnostics of a WN2-Type Major Sudden Stratospheric Warming Event in February 2018 Using a New Three-Dimensional Wave Activity Flux, Journal of Geophysical Research-Atmospheres, 124, 6120–6142, https://doi.org/10.1029/2018jd030162, 2019.

Harvey, V. L., Aggarwal, D., Becker, E., Bittner, M., Funke, B., Goncharenko, L., Jia, J., Lieberman, R., Liu, H. L., Maliniemi, V., Marchaudon, A., Nesse, H., Partamies, N., Pedatella, N., Schmidt, C., Shi, G., Stephan, C. C., Stober, G., van Caspel, W., Wüst, S., and Yamazaki, Y.: Signatures of Polar Vortex Weakening in the MLTI: A Review, Surveys in Geophysics, https://doi.org/10.1007/s10712-025-09899-3, 2025.

Hitchman, M. H., Gille, J. C., Rodgers, C. D., and Brasseur, G.: The Separated Polar Winter Stratopause - a Gravity-Wave Driven Climatological Feature, Journal of the Atmospheric Sciences, 46, 410–422, https://doi.org/10.1175/1520-0469(1989)046<0410:Tspwsa>2.0.Co;2, 1989.

Holt, L. A., Alexander, M. J., Coy, L., Liu, C., Molod, A., Putman, W., and Pawson, S.:

827 An evaluation of gravity waves and gravity wave sources in the Southern
828 Hemisphere in a 7 km global climate simulation, Q J R Meteorol Soc, 143, 2481–
829 2495, https://doi.org/10.1002/qj.3101, 2017.
830 Jones, M., Drob, D. P., Siskind, D. E., McCormack, J. P., Maute, A., McDonald, S. E.,
831 and Dymond, K. F.: Evaluating Different Techniques for Constraining Lower
832 Atmospheric Variability in an Upper Atmosphere General Circulation Model: A
833 Case Study During the 2010 Sudden Stratospheric Warming, Journal of Advances
834 in Modeling Earth Systems, 10, 3076–3102,
835 https://doi.org/10.1029/2018ms001440, 2018.
836 Karpechko, A. Y., Charlton-Perez, A., Balmaseda, M., Tyrrell, N., and Vitart, F.:
837 Predicting Sudden Stratospheric Warming 2018 and Its Climate Impacts With a
838 Multimodel Ensemble, Geophysical Research Letters, 45, 13538–13546,
839 https://doi.org/10.1029/2018gl081091, 2018.
840 Kodera, K., Mukougawa, H., and Itoh, S.: Tropospheric impact of reflected planetary
841 waves from the stratosphere, Geophysical Research Letters, 35,
842 https://doi.org/10.1029/2008gl034575, 2008.
843 Kumar, A., Krishna, M. V. S., and Ranjan, A. K.: Effect of 2009 Major SSW Event on
844 the Mesospheric CO2 Cooling, Journal of Geophysical Research-Atmospheres,
845 129, https://doi.org/10.1029/2024JD041298, 2024.
846 Kurihara, J., Ogawa, Y., Oyama, S., Nozawa, S., Tsutsumi, M., Hall, C. M., Tomikawa,
847 Y., and Fujii, R.: Links between a stratospheric sudden warming and thermal
848 structures and dynamics in the high-latitude mesosphere, lower thermosphere, and
849 ionosphere, Geophysical Research Letters, 37,
850 https://doi.org/10.1029/2010gl043643, 2010.
851 Lee, W., Song, I. S., Kim, J. H., Kim, Y. H., Jeong, S. H., Eswaraiah, S., and Murphy,
852 D. J.: The Observation and SD-WACCM Simulation of Planetary Wave Activity
853 in the Middle Atmosphere During the 2019 Southern Hemispheric Sudden
854 Stratospheric Warming, Journal of Geophysical Research-Space Physics, 126,
855 https://doi.org/10.1029/2020JA029094, 2021.
856 Li, K. F., Cageao, R. P., Karpilovsky, E. M., Mills, F. P., Yung, Y. L., Margolis, J. S.,
857 and Sander, S. P.: OH column abundance over Table Mountain Facility, California:

AM-PM diurnal asymmetry - art. no. L13813, Geophysical Research Letters, 32, https://doi.org/10.1029/2005gl022521, 2005.

Limpasuvan, V., Orsolini, Y. J., Chandran, A., Garcia, R. R., and Smith, A. K.: On the composite response of the MLT to major sudden stratospheric warming events with elevated stratopause, Journal of Geophysical Research-Atmospheres, 121, 4518–4537, https://doi.org/10.1002/2015jd024401, 2016.

Limpasuvan, V., Richter, J., Orsolini, Y., Stordal, F., and Kvissel, O.: The roles of planetary and gravity waves during a major stratospheric sudden warming as characterized in WACCM, JOURNAL OF ATMOSPHERIC AND SOLAR-TERRESTRIAL PHYSICS, 78-79, 84–98, https://doi.org/10.1016/j.jastp.2011.03.004, 2012.

Limpasuvan, V., Alexander, M. J., Orsolini, Y. J., Wu, D. L., Xue, M., Richter, J. H., and Yamashita, C.: Mesoscale simulations of gravity waves during the 2008-2009 major stratospheric sudden warming, Journal of Geophysical Research-Atmospheres, 116, https://doi.org/10.1029/2010jd015190, 2011.

Liu, H. L. and Roble, R. G.: Dynamical coupling of the stratosphere and mesosphere in the 2002 Southern Hemisphere major stratospheric sudden warming - art. no. L13804, Geophysical Research Letters, 32, https://doi.org/10.1029/2005gl022939, 2005.

Liu, H. L., Bardeen, C. G., Foster, B. T., Lauritzen, P., Liu, J., Lu, G., Marsh, D. R., Maute, A., McInerney, J. M., and Pedatella, N. M.: Development and validation of the whole atmosphere community climate model with thermosphere and ionosphere extension (WACCM-X 2.0), Journal of Advances in Modeling Earth Systems, 10, 381–402, https://doi.org/10.1002/2017MS001232, 2018.

Liu, X., Xu, J. Y., Yue, J., Vadas, S. L., and Becker, E.: Orographic Primary and Secondary Gravity Waves in the Middle Atmosphere From 16-Year SABER Observations, Geophysical Research Letters, 46, 4512–4522, https://doi.org/10.1029/2019gl082256, 2019.

Lu, Q., Rao, J., Liang, Z., Guo, D., Luo, J., Liu, S., Wang, C., and Wang, T.: The sudden stratospheric warming in January 2021, Environmental Research Letters, 16, https://doi.org/10.1088/1748-9326/ac12f4, 2021.

Lukianova, R., Kozlovsky, A., Shalimov, S., Ulich, T., and Lester, M.: Thermal and dynamical perturbations in the winter polar mesosphere-lower thermosphere region associated with sudden stratospheric warmings under conditions of low solar activity, Journal of Geophysical Research-Space Physics, 120, 5226–5240, https://doi.org/10.1002/2015ja021269, 2015.

Ma, Z., Gong, Y., Zhang, S., Zhou, Q., Huang, C., Huang, K., Luo, J., Yu, Y., and Li, G.: Study of a Quasi 4-Day Oscillation During the 2018/2019 SSW Over Mohe, China, JOURNAL OF GEOPHYSICAL RESEARCH-SPACE PHYSICS, 125, https://doi.org/10.1029/2019JA027687, 2020.

Manney, G. L., Schwartz, M. J., Krüger, K., Santee, M. L., Pawson, S., Lee, J. N., Daffer, W. H., Fuller, R. A., and Livesey, N. J.: Aura Microwave Limb Sounder observations of dynamics and transport during the record-breaking 2009 Arctic stratospheric major warming, Geophysical Research Letters, 36, https://doi.org/10.1029/2009gl038586, 2009.

Manney, G. L., Krüger, K., Pawson, S., Minschwaner, K., Schwartz, M. J., Daffer, W. H., Livesey, N. J., Mlynczak, M. G., Remsberg, E. E., Russell, J. M., and Waters, J. W.: The evolution of the stratopause during the 2006 major warming:: Satellite data and assimilated meteorological analyses, Journal of Geophysical Research-Atmospheres, 113, https://doi.org/10.1029/2007jd009097, 2008.

Marsh, D. R., Smith, A. K., Mlynczak, M. G., and Russell, J. M.: SABER observations of the OH Meinel airglow variability near the mesopause, Journal of Geophysical Research-Space Physics, 111, https://doi.org/10.1029/2005ja011451, 2006.

Maute, A., Hagan, M. E., Richmond, A. D., and Roble, R. G.: TIME- GCM study of the ionospheric equatorial vertical drift changes during the 2006 stratospheric sudden warming, Journal of Geophysical Research-Space Physics, 119, 1287–1305, https://doi.org/10.1002/2013ja019490, 2014.

McInturff, R. M.: Stratospheric warmings: Synoptic, dynamic and general-circulation aspects, 1978.

Medvedeva, I. V., Semenov, A. I., Pogoreltsev, A. I., and Tatarnikov, A. V.: Influence of sudden stratospheric warming on the mesosphere/lower thermosphere from the hydroxyl emission observations and numerical simulations, Journal of

Atmospheric and Solar-Terrestrial Physics, 187, 22–32, https://doi.org/10.1016/j.jastp.2019.02.005, 2019.

Minschwaner, K., Manney, G. L., Wang, S. H., and Harwood, R. S.: Hydroxyl in the stratosphere and mesosphere - Part 1: Diurnal variability, Atmospheric Chemistry and Physics, 11, 955–962, https://doi.org/10.5194/acp-11-955-2011, 2011.

Molod, A., Takacs, L., Suarez, M., and Bacmeister, J.: Development of the GEOS-5 atmospheric general circulation model: evolution from MERRA to MERRA2, Geoscientific Model Development, 8, 1339–1356, https://doi.org/10.5194/gmd-8-1339-2015, 2015.

Okui, H., Sato, K., Koshin, D., and Watanabe, S.: Formation of a Mesospheric Inversion Layer and the Subsequent Elevated Stratopause Associated With the Major Stratospheric Sudden Warming in 2018/19, Journal of Geophysical Research-Atmospheres, 126, https://doi.org/10.1029/2021JD034681, 2021.

Orsolini, Y. J., Zhang, J. R., and Limpasuvan, V.: Abrupt Change in the Lower Thermospheric Mean Meridional Circulation During Sudden Stratospheric Warmings and Its Impact on Trace Species, Journal of Geophysical Research-Atmospheres, 127, https://doi.org/10.1029/2022JD037050, 2022.

Orsolini, Y. J., Urban, J., Murtagh, D. P., Lossow, S., and Limpasuvan, V.: Descent from the polar mesosphere and anomalously high stratopause observed in 8 years of water vapor and temperature satellite observations by the Odin Sub-Millimeter Radiometer, Journal of Geophysical Research-Atmospheres, 115, https://doi.org/10.1029/2009jd013501, 2010.

Qin, Y. S., Gu, S. Y., Dou, X. K., and Wei, Y. F.: Unexpected Global Structure of Quasi-4-Day Wave With Westward Zonal Wavenumber 2 During the February 2023 Unusual Major Sudden Stratospheric Warming With Elevated Stratopause, Geophysical Research Letters, 51, https://doi.org/10.1029/2024GL109682, 2024.

Rao, J., Garfinkel, C. I., Chen, H. S., and White, I. P.: The 2019 New Year Stratospheric Sudden Warming and Its Real-Time Predictions in Multiple S2S Models, Journal of Geophysical Research-Atmospheres, 124, 11155–11174, https://doi.org/10.1029/2019jd030826, 2019.

Rhodes, C. T., Limpasuvan, V., and Orsolini, Y. J.: Eastward-Propagating Planetary

951 Waves Prior to the January 2009 Sudden Stratospheric Warming, Journal of
952 Geophysical Research-Atmospheres, 126, https://doi.org/10.1029/2020JD033696,
953 2021.
954 Richter, J. H., Sassi, F., and Garcia, R. R.: Toward a Physically Based Gravity Wave
955 Source Parameterization in a General Circulation Model, Journal of the
956 Atmospheric Sciences, 67, 136–156, https://doi.org/10.1175/2009jas3112.1, 2010.
957 Salinas, C. C. J. H., Wu, D. L., Lee, J. N., Chang, L. C., Qian, L. Y., and Liu, H. L.:
958 Aura/MLS observes and SD-WACCM-X simulates the seasonality, quasi-biennial
959 oscillation and El Nino-Southern Oscillation of the migrating diurnal tidedriving
960 upper mesospheric CO primarily through vertical advection, Atmospheric
961 Chemistry and Physics, 23, 1705–1730, https://doi.org/10.5194/acp-23-1705-
962 2023, 2023.
963 Sassi, F. and Liu, H. L.: Westward traveling planetary wave events in the lower
964 thermosphere during solar minimum conditions simulated by SD-WACCM-X,
965 Journal of Atmospheric and Solar-Terrestrial Physics, 119, 11–26,
966 https://doi.org/10.1016/j.jastp.2014.06.009, 2014.
967 Schneider, H., Wendt, V., Banys, D., Hansen, M., Clilverd, M., and Verronen, P. T.:
968 Impact of Sudden Stratospheric Warming and Elevated Stratopause Events on the
969 Very Low Frequency Radio Signal, Journal of Geophysical Research-Space
970 Physics, 130, https://doi.org/10.1029/2024JA033320, 2025.
971 Shapiro, A., Rozanov, E., Shapiro, A., Wang, S., Egorova, T., Schmutz, W., and Peter,
972 T.: Signature of the 27-day solar rotation cycle in mesospheric OH and H2O
973 observed by the Aura Microwave Limb Sounder, ATMOSPHERIC CHEMISTRY
974 AND PHYSICS, 12, 3181–3188, https://doi.org/10.5194/acp-12-3181-2012, 2012.
975 Stray, N., Orsolini, Y., Espy, P., Limpasuvan, V., and Hibbins, R.: Observations of
976 planetary waves in the mesosphere-lower thermosphere during stratospheric
977 warming events, ATMOSPHERIC CHEMISTRY AND PHYSICS, 15, 4997–5005,
978 https://doi.org/10.5194/acp-15-4997-2015, 2015.
979 Teng, C., Gu, S., Qin, Y., Dou, X., Li, N., and Tang, L.: Unexpected Decrease in TW3
980 Amplitude During Antarctic Sudden Stratospheric Warming Events as Revealed
981 by SD-WACCM-X, JOURNAL OF GEOPHYSICAL RESEARCH-SPACE

PHYSICS, 126, https://doi.org/10.1029/2020JA029050, 2021.

Tweedy, O., Limpasuvan, V., Orsolini, Y., Smith, A., Garcia, R., Kinnison, D., Randall, C., Kvissel, O., Stordal, F., Harvey, V., and Chandran, A.: Nighttime secondary ozone layer during major stratospheric sudden warmings in specified-dynamics WACCM, JOURNAL OF GEOPHYSICAL RESEARCH-ATMOSPHERES, 118, 8346–8358, https://doi.org/10.1002/jgrd.50651, 2013.

WEHRBEIN, W. and LEOVY, C.: AN ACCURATE RADIATIVE HEATING AND COOLING ALGORITHM FOR USE IN A DYNAMICAL MODEL OF THE MIDDLE ATMOSPHERE, JOURNAL OF THE ATMOSPHERIC SCIENCES, 39, 1532–1544, https://doi.org/10.1175/1520-0469(1982)039<1532:AARHAC>2.0.CO;2, 1982.

Winick, J., Wintersteiner, P., Picard, R., Esplin, D., Mlynczak, M., Russell, J., and Gordley, L.: OH layer characteristics during unusual boreal winters of 2004 and 2006, JOURNAL OF GEOPHYSICAL RESEARCH-SPACE PHYSICS, 114, https://doi.org/10.1029/2008JA013688, 2009.

Xu, J., Smith, A., Jiang, G., Gao, H., Wei, Y., Mlynczak, M., and Russell, J.: Strong longitudinal variations in the OH nightglow, GEOPHYSICAL RESEARCH LETTERS, 37, https://doi.org/10.1029/2010GL043972, 2010.

Yang, J., Wang, J., Liu, D., Guo, W., and Zhang, Y.: Observation and simulation of neutral air density in the middle atmosphere during the 2021 sudden stratospheric warming event, ATMOSPHERIC CHEMISTRY AND PHYSICS, 24, 10113–10127, https://doi.org/10.5194/acp-24-10113-2024, 2024.

Yue, X., Schreiner, W., Lei, J., Rocken, C., Hunt, D., Kuo, Y., and Wan, W.: Global ionospheric response observed by COSMIC satellites during the January 2009 stratospheric sudden warming event, JOURNAL OF GEOPHYSICAL RESEARCH-SPACE PHYSICS, 115, https://doi.org/10.1029/2010JA015466, 2010.

Zhang, J., Limpasuvan, V., Orsolini, Y., Espy, P., and Hibbins, R.: Climatological Westward-Propagating Semidiurnal Tides and Their Composite Response to Sudden Stratospheric Warmings in SuperDARN and SD-WACCM-X, JOURNAL OF GEOPHYSICAL RESEARCH-ATMOSPHERES, 126,

https://doi.org/10.1029/2020JD032895, 2021.

Zhang, J. R., Oberheide, J., Pedatella, N. M., and Liu, G. P.: Impact of Arctic and Antarctic Sudden Stratospheric Warmings on Thermospheric Composition, Journal of Geophysical Research-Space Physics, 130, https://doi.org/10.1029/2024JA032562, 2025.